Available online at www.sciencedirect.com

jmr&t Journal of Materials Research and Technology

journal homepage: www.elsevier.com/locate/jmrt

Original Article

# Effect of the amapá-latex chelating agent contents on the microstructure and photocatalytic properties of ZnO nanoparticles

Robert S. Matos [a,b,c,*], John M. Attah-Baah [c,d], Michael D.S. Monteiro [c], Benilde F.O. Costa [e], Marcelo A. Mâcedo [c,d], Romualdo S. Silva Junior [c,d], Henrique D. da Fonseca Filho [f], Rosane M.P.B. Oliveira [a], Nilson S. Ferreira [c,d,**]

[a] Postgraduate Program in Materials Science and Engineering ($P^2$CEM), Federal University of Sergipe, São Cristovão 49100-000, SE, Brazil
[b] Amazonian Materials Group, Federal University of Amapá (UNIFAP), Macapá, AP, Brazil
[c] Laboratory of Corrosion and Nanotechnology (LCNT), Federal University of Sergipe, 49100-000, São Cristovão, SE, Brazil
[d] Department of Physics, Federal University of Sergipe, 49100-000, São Cristovão, SE, Brazil
[e] University of Coimbra, CFisUC, Department of Physics, P-3004-516 Coimbra, Portugal
[f] Federal University of Amazonas-UFAM, Laboratory of Synthesis of Nanomaterials and Nanoscopy (LSNN), Physics Department, Manaus, Amazonas, Brazil

ARTICLE INFO

*Article history:*
Received 28 September 2022
Accepted 19 December 2022
Available online 23 December 2022

*Keywords:*
Amapá-latex
Zinc oxide
Nanoparticles
Photocatalytic activity

ABSTRACT

Herein, we have explored the defects-driven photocatalytic properties of ZnO nanoparticles synthesized using different sweet Amapá-latex contents as natural chelating agents. XRD, SAED, and FTIR analyses confirmed the formation of single-phase ZnO nanoparticles. TEM analysis showed nanoparticles with strong polycrystalline nature and average particle size ranging from 14.1 to 16.5 nm, with the smaller particle size (ZnO#10) exhibiting a larger surface area. The pentacyclic triterpenes present in Amapá-latex chelating agents play a critical role in the complexation of $Zn^{2+}$ ions and the formation of pure ZnO nanostructures. The broad photoluminescence spectra revealed several structural defects in the nanoparticles, particularly, $V_{Zn}$, $V_O^{++}$, $O_i^+$, and $Zn_O$ were widely observed for the sample synthesized using 10 mL of Amapá-latex (ZnO#10). A 99.47% visible-light-mediated discoloration of the aqueous methylene blue dye solution containing ZnO#10 nanoparticles was mainly ascribed to the continuous production of hydroxyl radicals by the defective structure of this sample. Furthermore, a ~30% TOC removal was observed after the 5th cycle of reuse of ZnO#10 nanoparticles, proving that the production of reactive species cleaves and breaks down MB dye molecules. Thus, the sweet Amapá-latex proved to be an effective chelating agent for obtaining ZnO nanoparticles with singular optical-structural characteristics that can be useful for treating dye-contaminated textile effluents.


* Corresponding author.
** Corresponding author.
E-mail addresses: robert_fisic@unifap.br (R.S. Matos), nilson@academico.ufs.br (N.S. Ferreira).
https://doi.org/10.1016/j.jmrt.2022.12.119

## 1. Introduction

ZnO nanoparticles are extensively studied due to their stable and non-cytotoxic characteristics, allowing their use in some technological fields, e.g., biomedical [1], solar cells [2,3], and photocatalysis [4,5]. For instance, in photocatalysis, the performance of ZnO nanoparticles is strongly dependent on their structural, morphological, and optical properties [6]. Indeed, in this field, there is a dependence on the interaction of ZnO with visible light, where the shape and particle size are considered the main attributes that directly influence their performance [7]. Furthermore, it is known that in most cases, ZnO is self-assembled with several inherent structural defects that tune its physical properties [8] and adequately dictate its application as a photocatalyst.

Wurtzite-like ZnO is one of the most common photocatalysts used to degrade harmful dyes from textile effluents [9]. In addition, some recent works have proved that the ZnO can be used for the discoloration of AZO dyes, such as methylene blue (MB) [10,11], methyl orange [12,13], and rhodamine B [14,15]. Recently, the improved performance of ZnO nanoparticles as photocatalysts has been attributed to the tunning of their optical bandgap by self-assembled structural defects like zinc vacancy ($V_{Zn}$), oxygen vacancy ($V_O$), single ionized oxygen vacancy ($V_O^+$), and double ionized oxygen vacancy ($V_O^{++}$) [16,17]. These structural defects create new energy levels in the optical bandgap, enhancing their electrical and optical properties [18]. Furthermore, they can also trap charge carriers delaying their recombination and improving the photocatalytic performance of the material.

The controlled-synthesis of ZnO nanoparticles have been a suitable way to identify better physical properties that improve their photocatalytic application. However, some convenient synthesis routes, such as precipitation and chemical reduction [19,20], are expensive, unsafe, and non-eco-friendly because they involve hazardous chemical chelating agents [21]. This problem has been overcome with the help of natural substances that provide a safe and eco-friendly chemical environment for obtaining ZnO nanoparticles [22,23]. Our previous work [17] investigated the photocatalytic activity of distinctively shaped ZnO nanoparticles synthesized using latex extracted from Amazon endemic plants, *Brosimum parinariodides* (sweet Amapá-latex) and *Parahancornia amapa*. We demonstrated that the chemical environment of sweet Amapá-latex is composed essentially of cycloeucalenol and obtusifoliol, which play a critical role in obtaining high-quality crystalline ZnO nanoparticles. These organic compounds can act by providing a favorable chemical environment for forming ZnO nanoparticles with different structural properties that can accelerate and improve the chemical reactions that lead to the generation of reactive chemical species for the destruction of AZO dye molecules in an aqueous solution. For these reasons, a comprehensive study on the influence of different volumes of sweet Amapá-latex on the physical properties of ZnO nanoparticles may reveal the potential of the biochelating agent as a precursor of nanostructures with enhanced photocatalytic properties for affordable wastewater decontamination.

The present study investigates the photocatalytic properties of ZnO nanoparticles synthesized using different contents of sweet Amapá-latex chelating agent. The influence of sweet Amapá-latex on the structural, microstructural, and optical properties was successfully investigated. Our photocatalytic experiments evaluated the MB dye discoloration in aqueous solutions under visible light.

## 2. Material and methods

### 2.1. Synthesis of the nanoparticles

The sweet Amapá-latex chelating agent used in our synthesis was collected at 0°52′25″S and 52°24′06″W. In an easy and safe procedure, 0.0025 mols of zinc nitrate ($Zn(NO_3)_2 \cdot 6H_2O$) (Sigma-Aldrich, purity ≥99%) was solubilized in 5 mL (ZnO#5), 10 mL (ZnO#10), and 15 mL (ZnO#15) of Amapá-latex under magnetic stirring for 30 min. The precursor solutions were kept at 100 °C overnight to obtain the amorphous black xerogels. Finally, the xerogels were calcined at 500 °C and quenched after 1 h to get ZnO nanopowders.

### 2.2. Characterization

The chemical functional groups present in the amorphous xerogels and ZnO nanopowders were investigated using a Fourier transform infrared (FTIR) spectrometer (PerkinElmer Spectrum Two™), operating at 4000–400 $cm^{-1}$ and resolution of 8 $cm^{-1}$, using KBr pellets. The thermal decomposition of the amorphous xerogels was performed in a thermogravimetric apparatus (Shimadzu TGA-50) operating at 25–1000 °C and a heating rate of 10 °C.$min^{-1}$. The structural analysis of ZnO nanoparticles was carried out in an X-ray diffractometer (Empyrean, PANalytical) using a Co X-ray tube ($K_{\alpha 1}$ = 1.78901 Å), operating of 2θ = 20°–90°, 40 kV, and step size of 2θ = 0.01°. All obtained XRD patterns were refined by the Rietveld method using a Thompson-Cox-Hastings pseudo-Voigt function whose refinement program was implemented in the Fullprof suite package [24]. The broadening effects were accessed by a resolution function using a lanthanum hexaboride ($LaB_6$) pattern (NIST/SRM 660). Finally, the angular dependence of the full width at half maximum (β), anisotropy of the peak broadening profile, the average crystallite size ($D_{XRD}$), and strain broadening anisotropy were described or calculated using a spherical harmonic model (SPH) according to our previous procedure [25]. The morphology and selected area electron diffraction patterns (SAED) of ZnO nanoparticles were investigated by a transmission electron microscope (TEM) (JEOL 2100) operating at 220 kV. The pore volume and surface area of ZnO nanoparticles were determined by a Quantachrome NOVAtouch adsorption-desorption (NOVAtouch 1200e, Anton Paar QuantaTec Inc.) apparatus. The nature of ZnO nanoparticles' optical absorption and their structural defects were investigated by diffuse reflectance

ultraviolet spectroscopy (DRUV) and photoluminescence (PL) using the Ocean Optics HR2000 and Jasco FP-8600 spectrophotometers, operating on 200–800 nm.

### 2.3. Photocatalytic experiments

The degradation of methylene blue (MB) dye in an aqueous solution (10 mg $L^{-1}$) in the presence of ZnO nanoparticles was investigated using a typical photocatalytic experiment. First, the initial stable MB solution was obtained [25]. Subsequently, 10 mg of ZnO nanoparticles were suspended in 50 mL of the MB solution and kept under stirring for 5 min for a suitable adsorption-desorption equilibrium of MB dye molecules. The resultant suspension was irradiated with visible light using a 600-W halogen lamp (7.74 W $m^{-2}$) for 240 min. An identical ZnO#10 sample experiment was used in the dark as a control experiment (CE). Approximately 3 mL of the irradiated and non-irradiated suspensions were collected at intervals of 20 min to measure the maximum absorbance of MB dye at $\lambda_{max} = 664$ nm using a UV–vis spectrophotometer (VARIAN, Cary 100). The total discoloration of MB dye was determined by Eq. (1), and the Foto-Fenton reaction kinetic was estimated using a Langmuir–Hinshelwood kinetic model (Eq. (2)).

$$\%\ \text{Discoloration} = \left(\frac{C_0 - C}{C_0}\right) \times 100\% = \left(\frac{A_0 - A}{A_0}\right) \times 100\% \quad (1)$$

$$kt = -\ln\left(\frac{C}{C_0}\right) \quad (2)$$

where $A_0$ and $C_0$ are the absorption and equilibrium concentration initial at 664 nm at t = 0 min, respectively, A and C are the absorption and equilibrium concentration final at 664 nm after t = 240 min of irradiation with visible light, and k is the pseudo-first-order rate constant. Additionally, an elemental trapping experiment (ETE) and total organic carbon (TOC) test were performed to investigate the chemical species responsible for the destruction of MB molecules and their mineralization efficiency, respectively. The typical ETE was performed using 3 mL of isopropanol (IPA) (Sigma-Aldrich, ≥99.5%), 0.1 mmol of benzoquinone (BQ) (Sigma-Aldrich, ≥98%), and 0.1 mmol of disodium ethylenediaminetetraacetate dihydrate (EDTA) (Sigma-Aldrich, ≥99%) as scavengers. The mineralization efficiency (η) of MB organic molecules was computed according to Eq. (3) using the total organic carbon before ($T_o$) and after (T) the photocatalytic process as a function of irradiation time, measured in a thermoreactor (Analytik Jena, Model NC 3100).

$$\eta(\%) = \left(1 - \frac{T}{T_0}\right) \times 100\% \quad (3)$$

## 3. Results and discussion

### 3.1. Xerogels analysis

Before the calcination procedure, the chemical structure and thermal behavior of the obtained xerogels were carefully investigated, as shown in Fig. 1. FTIR spectra (Fig. 1(a)) reveals the functional groups present in the xerogels precursors of ZnO nanoparticles. In all xerogels, we computed a band around 3434 $cm^{-1}$ associated with the O–H stretching vibration linked to the hydration condition of the xerogels. The bands at 2931 $cm^{-1}$ and 2858 $cm^{-1}$ are related to C–H stretching vibrations ascribed to open-chain hydrocarbons in proteins and lipids [26] existing in the sweet Amapa-latex chelating agent. The interaction between $Zn^{2+}$ ions and alkenes π bonds promoted different oxidation-reduction processes during the $Zn^{2+}$ complexation, generating C–H bands with different intensities. At 1731 $cm^{-1}$, we can note a band relative to the C=O stretching vibration assigned to saturated aliphatic aldehydes [17]. The band positioned at 1731 $cm^{-1}$ arises from O–H's symmetric angular deformation due to water adsorbing on the surface of the xerogels [16]. The symmetrical and asymmetrical in-plane stretch vibration observed at 1532 $cm^{-1}$ and 1459 $cm^{-1}$ are ascribed to the COO ester groups [17], respectively. The band located at 1389 $cm^{-1}$ refers to asymmetric stretching of C–O, probably due to the presence of $CO_3^{2-}$ [27], whereas at 1232 $cm^{-1}$ is associated with the stretching vibration of C–N linked to amines [28]. The C–O–H vibrations recorded around 1065 $cm^{-1}$ are assigned to the undenatured carbohydrates [16]. Correspondingly, the weak bands at 890 $cm^{-1}$, 822 $cm^{-1}$, and 715 $cm^{-1}$ are associated with symmetric angular deformation of C–O and O–H and antisymmetric angular deformation of C–O, which are probably related to the existence of carbonates in the xerogels [16]. Furthermore, the weak band around 511 $cm^{-1}$ is assigned to the Zn–OH stretching vibration, suggesting a formation of an amorphous Zn-based complex. The $CO_3^{2-}$ band associated with carbonates was not observed in the spectrum of sweet Amapá-latex previously reported [17], indicating the formation of zinc carbonate. In this regard, previous works have shown that precursor complexes of ZnO nanoparticles obtained by green routes can be constituted mainly by hydrozincite ($Zn_5(CO_3)_2(OH)_6$) [29,30], a known carbonate. Thus, our chemical analysis suggests that the polymer matrix of Amapá-latex chelates the $Zn^{2+}$ ions, which probably form an amorphous complex rich in $Zn_5(CO_3)_2(OH)_6$.

The thermal decomposition of the xerogels was described according to TGA/DTG curves, whose results are shown in Fig. 1(b)–(d). As can be seen, all xerogels lost weight significantly from 25 to 1000 °C in a similar way. Still, differences were recorded due to the different hydration conditions and chemical composition of xerogels, as noted in the FTIR spectrum (Fig. 1(a)). Between 25 and ~230 °C, the xerogels lost 15% (ZnO#5), 11% (ZnO#10), and 16% (ZnO#15) of their total weight (Fig. 1(b)–(d)), where ZnO#10 exhibit an endothermic process positioned at approximately 175 °C, while ZnO#5 and ZnO#15 display two endothermic peaks at 130 and 198 °C, and, 172 and 212 °C, respectively. The endothermic peaks found at 25–200 °C can be assigned to the elimination of molecular water and gases adsorbed on the surface of the xerogels [16]. Moreover, they may also be associated with the denaturation of some biopolymers and proteins present in the Amapá-latex chelating agent. From 230 to 420 °C, there was the most significant weight loss of the xerogels, whose values were estimated to be 35% (ZnO#5), 62% (ZnO#10), and 60% (ZnO#15), which are also accompanied by intense endothermic peaks positioned at 350,

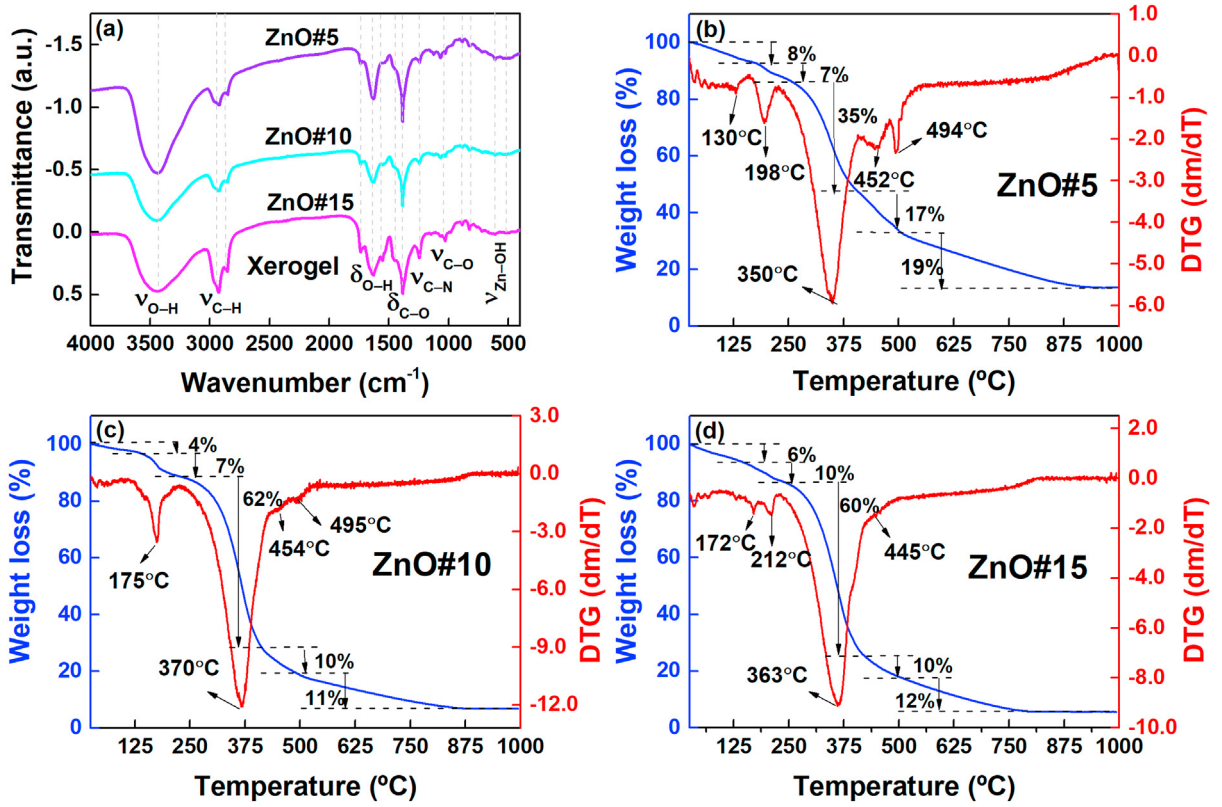


**Fig. 1 – (a) FTIR spectra and (c)–(d) TGA/DTG curves of the xerogels precursors of ZnO nanoparticles obtained with different contents of sweet Amapá-latex chelating agent.**

370, and 363 °C (Fig. 1(b)–(d)). This weight loss is ascribed to the robust decomposition of organic compounds of sweet Amapá-latex. According to Ferreira et al. [16], the complete conversion of the amorphous complex into $Zn_5(CO_3)_2(OH)_6$ occurs in this temperature range. Finally, from 420 to 1000 °C, the xerogels lost a total of 36% (ZnO#5), 21% (ZnO#10), and 22% (ZnO#15),

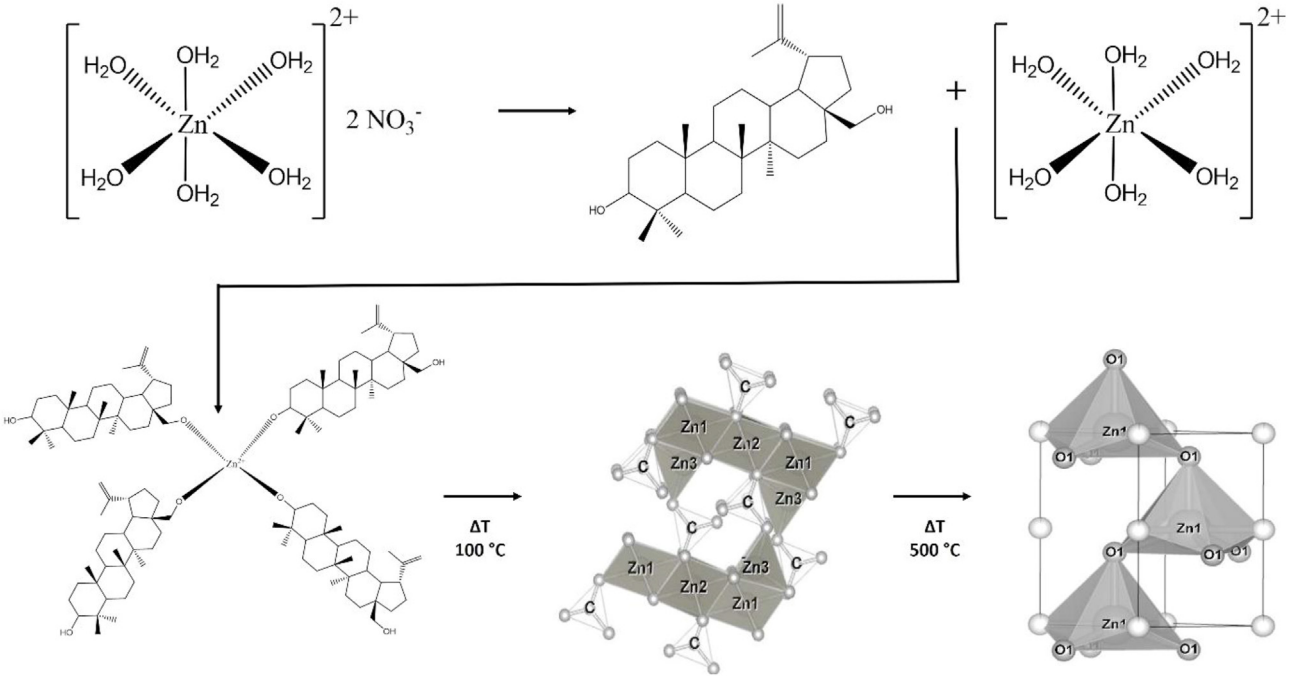


**Fig. 2 – The possible mechanism for forming ZnO nanoparticles using sweet Amapá-latex as an effective chelating agent.**

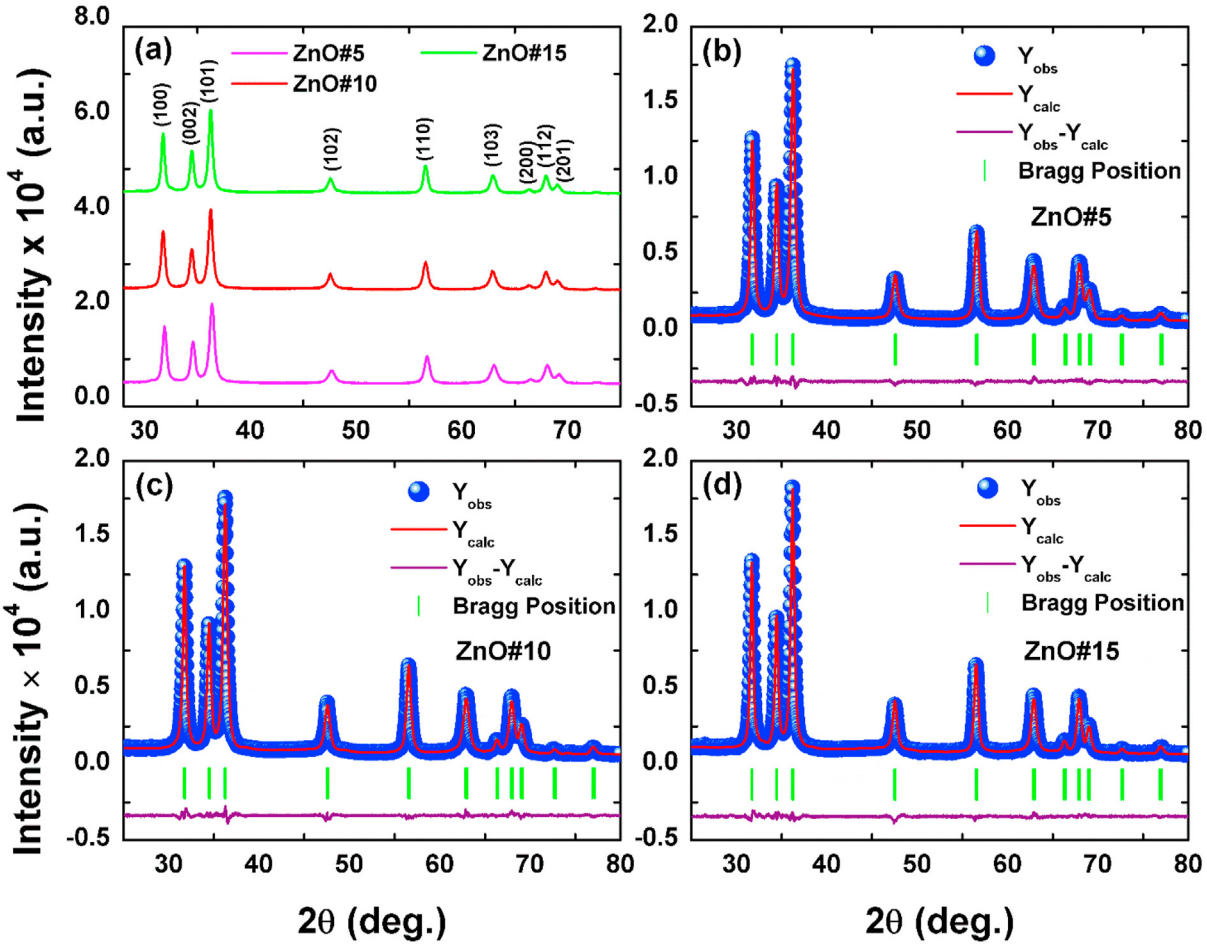


**Fig. 3 – (a) XRD patterns and (c)–(d) Rietveld refinements of ZnO nanoparticles calcined at 500 °C.**

where ZnO#5 and ZnO#10 show two endothermic peaks at 452 and 494 °C and 454 and 495 °C, respectively, while a weak peak at 445 °C was recorded for ZnO#15 (Fig. 1(b)–(d)). The peaks around 450 °C can be assigned to the release of $CO_2$ and $H_2O$ adsorbed on the surface of $Zn_5(CO_3)_2(OH)_6$, which is further completely decomposed into ZnO nanoparticles after around 490 °C. The weight losses recorded above 500 °C are attributed to the vigorous and persistent decomposition of $CO_2$ residual, indicating that this temperature is suitable for obtaining highly crystalline ZnO nanoparticles. Fig. 2 shows the probable mechanism for forming ZnO nanoparticles after the decomposition of $Zn_5(CO_3)_2(OH)_6$. Firstly, $Zn(NO_3)_2$ is solubilized in the Amapá-latex chelating agent, forming a hydrated complex (Eq. (4)). Subsequently, $Zn^{2+}$ ions interact with hydroxyls and alkenes molecules present in pentacyclic triterpenes compounds as suggested in our previous work [17]. Further, the metal chelation is stabilized by its constant interaction with the nucleophilic sites of triterpenes donor ligands. The heat treatment of the precursor solutions at 100 °C leads to the formation of amorphous xerogel rich in $Zn_5(CO_3)_2(OH)_6$ (Eq. (5)), which further is decomposed into ZnO nanoparticles at 500 °C (Eq. (6)).

$$Zn(NO_3)_2.6\,H_2O + 4\,ROH \xrightarrow[\Delta]{} [Zn(HOR)_4]^{2+} + 2\,NO_3^- + 6\,H_2O \quad (4)$$

$$[Zn(HOR)_4]^{2+} \xrightarrow[\Delta T=100\ ^\circ C]{} Zn_5(CO_3)_2(OH)_6 \quad (5)$$

$$Zn_5(CO_3)_2(OH)_6 \xrightarrow[\Delta T=500\ ^\circ C]{} ZnO \quad (6)$$

### 3.2. *Nanoparticles characterization*

The X-ray diffraction patterns of ZnO nanoparticles calcined at 500 °C as well as their respective Rietveld refinement are shown in Fig. 3. The reflections displayed in Fig. 3(a) are associated with the (110), (002), (101), (102), (110), (103), (200), (112), and (201) crystallographic planes assigned to the hexagonal wurtzite-like structure of ZnO (ICSD #82028) belonging to the $P6_3mc$ space group. The characteristics of the patterns prove that our ZnO nanopowders do not exhibit secondary phases and have high crystallinity, supporting the thermal analysis described by the TGA/DTG curves (Fig. 1(b)–(d)). Such behavior is supported by the Rietveld refinement (Fig. 3(b)–(d)), whose relevant parameters are summarized in Table S1. The well-fitted patterns ($\chi^2 \sim 2$) confirm the wurtzite structure of ZnO nanoparticles with small differences promoted by the different contents of the sweet Amapá-latex used in the synthesis. We recorded that $O^{2-}$ species occupy

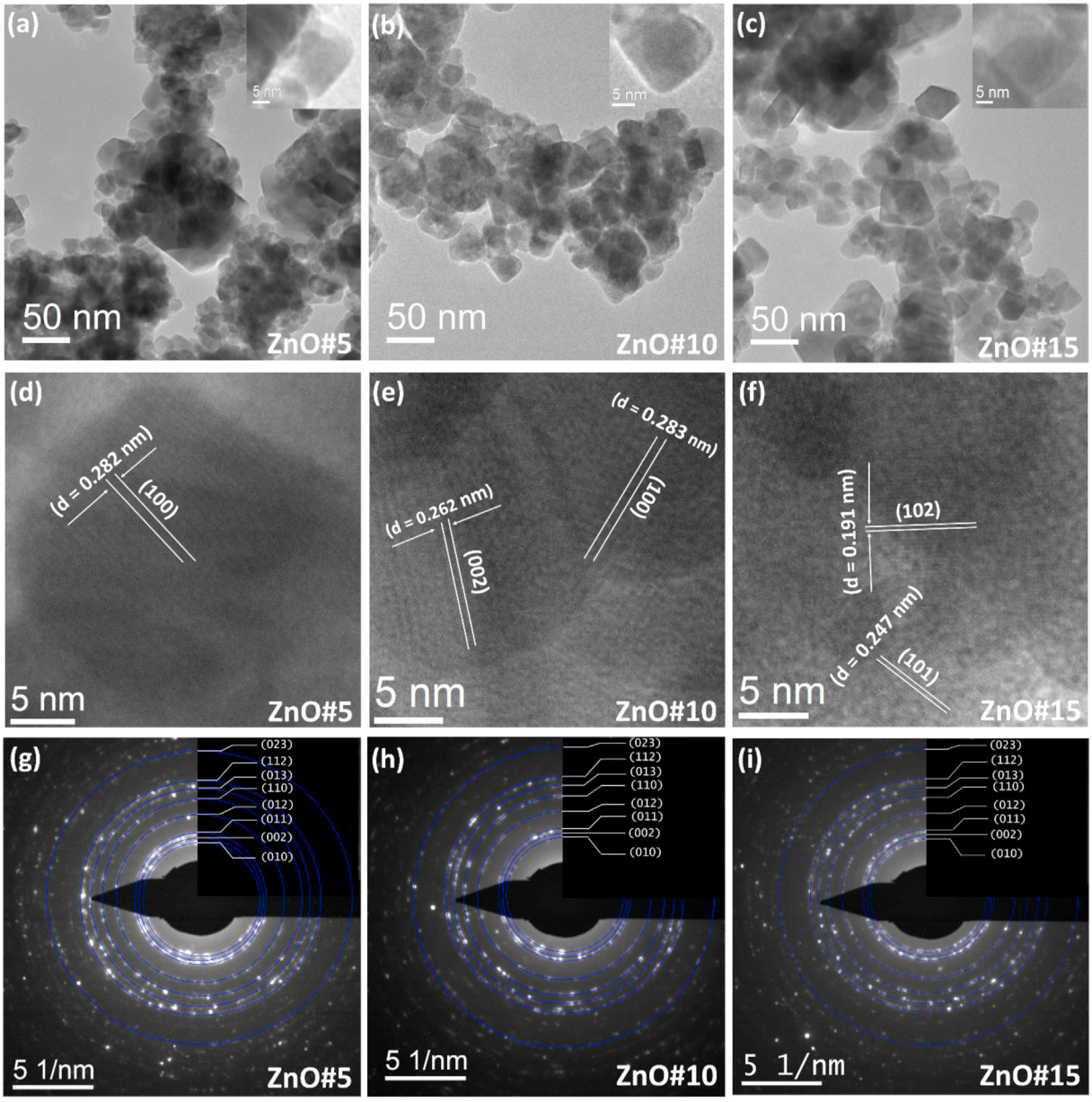


**Fig. 4 – (a)–(c) TEM images, (d)–(f) HRTEM images, and (g)–(i) SAED patterns of ZnO nanoparticles calcined at 500 °C.**

higher positions from ZnO#5 (0.3837 Å) to ZnO#15 (0.3837 Å), which promoted a small decrease in Zn–O bond length (BL) $\left(\frac{\Delta(BL)}{BL} = -0.00036\%\right)$ and bond angle (BA) $\left(\frac{\Delta(BA)}{BA} = -0.00248\%\right)$ (Table S1), generating small distortions in the crystal lattice. The BL values found are smaller than bulk ZnO (1.9778 Å), which can be attributed to the size confinement effect [31]. Such distortions modified the crystal lattice, generating an increase of a = b (3.2524–3.2561 Å) and a decrease of c (5.2052–5.2017 Å) from ZnO#5 to ZnO#15, also creating a cell expansion $\left(\frac{\Delta V}{V} = +0.00231\%\right)$ (Table S1). The average crystallite size ($D_{XRD}$) and lattice microstrain were calculated to be 13.82 nm and 0.072 (ZnO#5), 13.48 nm and 0.074 (ZnO#10), and 16.38 nm and 0.061 (ZnO#15), respectively. The small lattice distortions and crystallite size produced nanoparticles with different lattice microstrains [32], grain boundaries, and a defective structure.

The morphological and microstructural aspects of ZnO nanoparticles investigated by TEM and SAED aided in better understanding their crystalline characteristics. For example, TEM images (Fig. 4(a)-(c)) confirm that ZnO nanoparticles were estimated to be 15.17 nm (ZnO#5), 14.19 nm (ZnO#10), and 16.52 nm (ZnO#15) (Fig. S1), in a variety of shapes with a faceted surface such as spherical, cubic, hexagonal, and pentagonal. Furthermore, it was found that the ZnO nanoparticles tended to agglomerate strongly, which could be attributed to the high surface area and surface energy of the ZnO nanoparticles [33–35].

The polycrystalline behavior of the nanoparticles was investigated by HRTEM, as shown in Fig. 4(d)–(f). The crystallographic planes with different d-spacing (d) lattice fringes in different nanoparticles were found at: (100) (d = 0.282 nm) (ZnO#5) (Fig. 4(d)), (002) (d = 0.262 nm) and (100) (d = 0.283 nm) (ZnO#10) (Fig. 4(e)), and (102) (d = 0.191 nm) and (101) (d = 0.247 nm) (ZnO#15) (Fig. 4(f)). Moreover, the SAED patterns (Fig. 4(g)–(i)) reveal well-defined circular rings associated with the planes (023), (112), (013), (110), (012), (011), (002), and (010), which are indexed to the wurtzite structure of ZnO nanoparticles [16], confirming their polycrystalline nature.

The BET adsorption-desorption curves used to determine the surface area (SA) and pore volume (PV) of ZnO nanoparticles are shown in Fig. S2. The SA of the samples was determined to be 23.4 $m^2.g^{-1}$ (ZnO#5), 30.7 $m^2.g^{-1}$ (ZnO#10), and 7.6 $m^2.g^{-1}$ (ZnO#15). The PV was obtained as 0.0728 $cm^3.g^{-1}$ (ZnO#5), 0.107 $cm^3.g^{-1}$ (ZnO#10), and 0.0533 $cm^3.g^{-1}$ (ZnO#15). As can be seen, the SA and PV of ZnO#10 are higher than ZnO#5 and ZnO#15, which can be due to a more significant presence of capping agents adsorbed on their surface, as it is known that bioactive compounds can coat the surface of oxide nanoparticles increasing the surface area [11,36]. Moreover, the SA value of the ZnO#10 sample is also higher than those reported by other previous green synthesized ZnO nanoparticles photocatalysts, e.g., 16.27 $m^2.g^{-1}$ [37], 13.56 $m^2.g^{-1}$ [38], and 12.47 $m^2.g^{-1}$ [39].

The functional groups present in our ZnO nanoparticles calcined at 500 °C are highlighted in Fig. 5. The bands located at 435 $cm^{-1}$ and 412 $cm^{-1}$ are assigned to the stretch vibration of the Zn–O bond [40], confirming the formation of ZnO nanoparticles that are well supported by XRD (Fig. 3) and TEM (Fig. 4) analyses. The residual water adsorbed on the nanoparticle surface resulted in O–H bands positioned around 3370, 1634, and 807 $cm^{-1}$. However, the bands observed at 1192 $cm^{-1}$ (symmetrical stretch vibration of C–O), 870 $cm^{-1}$ (symmetrical out-of-plane angular deformation of C–O), and 1467 $cm^{-1}$ (stretch vibration of C=C) are ascribed to residual organic compounds adsorbed on the surface of the nanoparticles. Moreover, all nanoparticles also exhibit the band at 1388 $cm^{-1}$ due to the persistent presence of $CO_3^{2-}$ molecules. Additionally, the weak C–H bands positioned at 2932 and 2884 $cm^{-1}$ are observed only for ZnO#15. Thus, our chemical analysis indicates surface contamination of the nanoparticles, where the ZnO#15 sample exhibited the most extraordinary richness of residual organic structures, mainly $CO_2$ [16]. Despite that, our structural analysis showed no secondary phases, suggesting that the contribution of impurities to the final nanopowder constituent is negligible.

The defective structure of ZnO nanoparticles calcined at 500 °C was investigated by DRUV and photoluminescence measurements at room temperature, whose results are displayed in Fig. 6(a). It shows two DRUV absorption bands around 380 nm (strong) and ~510 nm (weak), which are assigned to the monodisperse nature of ZnO nanoparticles [41] and a transition O 2p → Zn 3 d [16,42], respectively. The weak bands expose a redshift due to intrinsic defects generated by interstitial oxygens $O_i$ [43]. The optical bandgap estimated from Tauc plots was found to be 2.88 eV (ZnO#5), 3.02 eV (ZnO#10), and 3.09 eV (ZnO#15) (Fig. S3), showing that

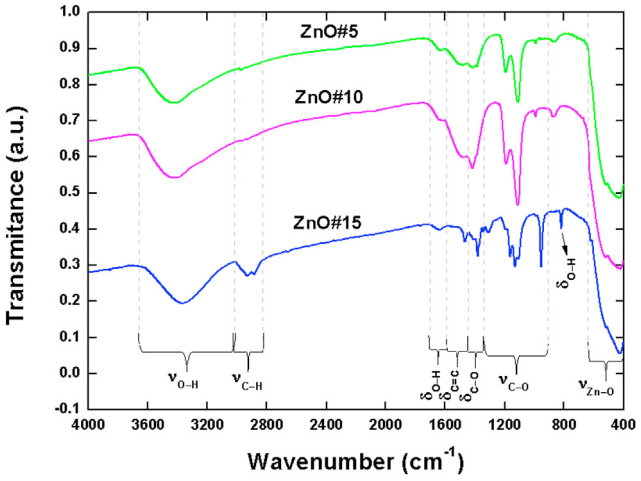


**Fig. 5 – FTIR spectra of ZnO nanoparticles calcined at 500 °C.**

the contents of Amapá-latex chelating agent play a vital role for adjusting the bandgap of ZnO nanoparticles. The higher intensity of DRUV bands in ZnO#5 and ZnO#10 indicate more significant amounts of intrinsic and planar defects in these nanoparticles [16], probably due to the higher lattice microstrain.

The room temperature PL spectra (Fig. 6(b)–(d)) reveal a broad line ranging from 372 to 700 nm for all nanoparticles, which is a characteristic of defect-rich ZnO nanoparticles [44]. From Table 1, we note that near-band-edge (NBE) emission exhibits a maximum displacement of 0.11 eV from ZnO#5 to ZnO#15, revealing an optical nature utterly different from the ZnO bulk. According to Ferreira et al. [16], ZnO bulk displays a stable excitonic state shifted below its conduction band (CB) at ~ 27 °C, in a bandgap range that can vary from 3.29 to 3.32 eV. Thus, ZnO#5 and ZnO#15 have NBE emissions positioned at notably longer wavelengths than ZnO bulk, showing a spectral diffusion due to exciton migration in nanoparticles synthesized with larger contents of sweet Amapá-latex chelating agent. These emissions can be assigned to transitions of the conduction band (CB) to the deep defect band [45], e.g., zinc vacancies ($V_{Zn}$) [46] or transitions from interstitial zinc ($Zn_i$) to VB ($Zn_i \rightarrow VB$) [47]. The violet emissions at ~418 nm (2.96 eV) recorded only for ZnO#5 and ZnO#10 are attributed to $V_{Zn}$ defects [48] or electronic transitions from shallow donor levels of $Zn_i$ to VB ($Zn_i \rightarrow VB$) [49]. For ZnO#15, the violet emission at ~414 nm can be ascribed to $V_{Zn}$ or electronic transitions from the donor level to VB ($e^- \rightarrow VB$) [50,51]. Blue emissions at ~440 nm (2.81 eV) (ZnO#5), ~444 nm (~2.79 eV) (ZnO#10), and ~445 nm (~2.79 eV) (ZnO#15) arise due to single ionized zinc vacancies ($V_{Zn}^{+}$) [52,53], electronic transitions from $Zn_i$ to VB ($Zn_i \rightarrow VB$) [54], and electronic transitions from CB to interstitial oxygen ($O_i$) (CB $\rightarrow O_i$) [54,55]. The blue emission located at ~452 nm (2.74 eV) is only observed for ZnO#10 and occurs due to electronic transitions from the shallow donor level of $Zn_i$ to $V_{Zn}$ ($Zn_i \rightarrow V_{Zn}$) [56,57]. Nonetheless, the blue emissions at ~471 nm (2.63 eV) (ZnO#5), ~472 nm (~2.62 eV) (ZnO#10), and ~467 nm (~2.65 eV) (ZnO#15) are associated with

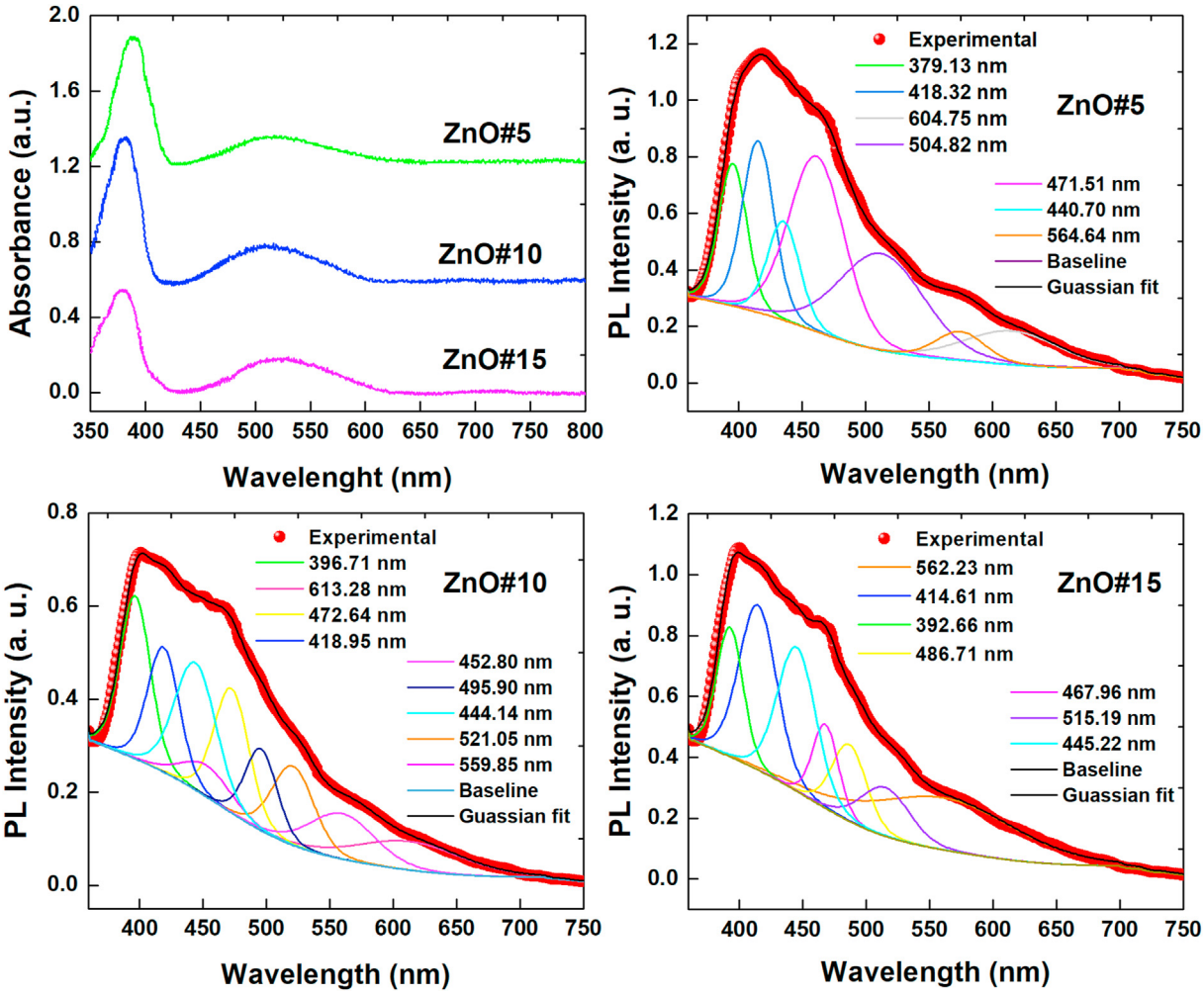


**Fig. 6 – Room temperature (a) DRUV absorption and (b)–(d) PL spectra of ZnO nanoparticles calcined at 500 °C.**

electron transitions from the donor level of single ionized oxygen vacancy $V_O^+$ to VB ($V_O^+ \rightarrow VB$) [58]. Additionally, ZnO#10 and ZnO#15 samples expose blue emitions at ~495 nm (~2.50 eV) and 486 nm (~2.55 eV), respectively, which are ascribed to doubly ionized oxygen vacancy ($V_O^{++}$) [59,60]. The green emissions at ~504 nm (2.46 eV) and 564 nm (2.20 eV) (ZnO#5), ~521 (2.38 eV) and 559 nm (2.21 eV) (ZnO#10), and ~515 (2.41 eV) and 562 nm (2.21 eV) (ZnO#15) have been consistently attributed to the presence of $V_O^+$ defect [61–77]. The orange emission at ~604 nm (2.05 eV) observed only for ZnO#5 is assigned to $V_O$ and $V_O^+$ [78,79], while for ZnO#10, there is an orange peak at ~613 nm (2.02 eV) due to the $O_i^+$ and $Zn_O$ defects [80,81]. As can be seen, our ZnO nanoparticles share several similar defects. Still, the coexistence of $V_{Zn}$, $V_O^{++}$, $O_i^+$, and $Zn_O$ defects was only recorded for the powder prepared with 10 mL of Amapá-latex chelating agent.

### 3.3. *Photocatalytic activity*

The MB discoloration photocatalytic experiments using ZnO nanoparticles as photocatalysts are shown in Fig. 7. The curves in Fig. 7(a) refer to the control experiment (CE) and reveal a slight reduction of the MB characteristic band at 664 nm. However, the experiments containing ZnO#5 (Fig. (b)), ZnO#10 (Fig. (c)), and ZnO#15 (Fig. (d)) nanoparticles display a substantial reduction of the MB band after irradiation with visible light, indicating that organic dye molecules are destructed in the aqueous solution, which is demonstrated by the evolution of the dye discoloration (inserted scheme) after 240 min of irradiation.

A more comprehensive study of the photocatalytic activity of ZnO nanoparticles based on their UV–vis spectra is shown in Fig. 8. After the adsorption-desorption equilibrium of MB dye molecules, the adsorption rates were determined to be 3.2% (CE), 6.3% (ZnO#5), 9.5% (ZnO#10), and 4.1% (ZnO#15). Under visible light irradiation, Fig. 8(a) reveal a more significant reduction of the $C/C_0$ factor in the experiments containing the ZnO nanoparticles after 240 min of exposure to visible light, indicating that they are enormously efficient for removing the MB dye. Moreover, our nanoparticles produced high MB discoloration rates compared to CE (Fig. 8(b)) at 93.89% (ZnO#5), 99.47% (ZnO#10), and 98.94% (ZnO#15) (Fig. 8(c)), whose reaction rates were estimated to be 0.0115,

**Table 1 – Peaks position, energy level, and defects obtained from the PL spectra analysis of ZnO nanoparticles calcined at 500 °C.**

| Sample | Peak Position (nm) | Energy Level (eV) | Defect | References |
|---|---|---|---|---|
| ZnO#5 | 379.13 | 3.27 | NBE | [54,82–84] |
| | 418.32 | 2.96 | $V_{Zn}$, $Zn_i \rightarrow VB$ | [49,85] |
| | 440.70 | 2.81 | $V_{Zn}^{+}$, $Zn_i \rightarrow VB$, $CB \rightarrow O_i$ | [52–55] |
| | 471.51 | 2.63 | $V_O^{+} \rightarrow VB$ | [58] |
| | 504.82 | 2.46 | $V_O^{+}$ | [61,62] |
| | 564.64 | 2.20 | $V_O^{+}$ | [70–72] |
| | 604.75 | 2.05 | $V_O$, $V_O^{+}$ | [78,79] |
| ZnO#10 | 396.71 | 3.13 | NBE | [82–84] |
| | 418.95 | 2.96 | $V_{Zn}$, $Zn_i \rightarrow VB$ | [49,85] |
| | 444.14 | 2.79 | $V_{Zn}^{+}$, $Zn_i \rightarrow VB$, $CB \rightarrow O_i$ | [52–55] |
| | 452.80 | 2.74 | $Zn_i \rightarrow V_{Zn}$ | [56,57] |
| | 472.64 | 2.62 | $V_O^{+} \rightarrow VB$ | [58] |
| | 495.90 | 2.50 | $V_O^{++}$ | [59,60] |
| | 521.05 | 2.38 | $V_O^{+}$ | [52,73,74] |
| | 559.85 | 2.21 | $V_O^{+}$ | [75–77] |
| | 613.28 | 2.02 | $O_i^{+}$, $Zn_O$ | [80,81] |
| ZnO#15 | 392.66 | 3.16 | NBE | [82–84] |
| | 414.61 | 2.99 | $V_{Zn}$, $e^{-} \rightarrow VB$ | [50,86,87] |
| | 445.22 | 2.79 | $V_{Zn}^{+}$, $Zn_i \rightarrow VB$, $CB \rightarrow O_i$ | [52–55] |
| | 467.96 | 2.65 | $V_O^{+} \rightarrow VB$ | [58] |
| | 486.71 | 2.55 | $V_O^{+}$ | [61,88] |
| | 515.19 | 2.41 | $V_O^{+}$ | [63–67] |
| | 562.23 | 2.21 | $V_O^{+}$ | [68,69] |

0.0174, and 0.0171 $min^{-1}$ (Fig. 8(d)), respectively. Table 2 compares the results found in the present work with those reported in the literature. In this regard, the photocatalytic efficiency of our nanoparticles is comparable with other photocatalysts used for the degradation of different organic molecules. It is worth noting that we maintain a low ratio between photocatalyst weight (PW) and dye concentration (DC) (1:1) compared to 2.5:1, 5:1, and 10:1 generally used by the previous works (Table 2). Thus, the increase of the PW:DC ratio can still promote greater photocatalytic efficiency of ZnO nanoparticles in a shorter irradiation time.

The stability of the photocatalytic process and chemical species responsible for the destruction of MB dyes molecules were known after a cyclic photodegradation experiment and an elemental trapping analysis, whose Uv–vis spectra are displayed in Fig. S4. Fig. 9(a) shows that ZnO#10 can be used for up to 4 degradation cycles without significant loss of photocatalytic performance. However, the total photocatalytic performance loss from the 1st → 5th cycle is only 14%, showing that the nanoparticles exhibit robust stability as photocatalysts after 5 cycles of recyclability. The progressive loss of photocatalytic performance from the 2nd → 5th cycle affected the photocatalytic reaction rate, which decreased from 0.0156 $min^{-1}$ to 0.0099 $min^{-1}$ (Fig. S5), showing that the degradation of the MB dye molecules occurs more slowly after the 2nd reuse cycle. After the 5th cycle of reuse, a TOC test was performed in all collected aliquots, which revealed a total mineralization of ~30% (Fig. 9(b)) of the MB dye molecules after 120 min of irradiation with visible light. Moreover, the mineralization process is intensified after 100 min of irradiation, suggesting that longer irradiation times can lead to the complete removal of organic carbon from the aqueous solution containing ZnO nanoparticles under visible light.

The elemental trapping analysis (Fig. 9(c)) showed that the addition of IPA in the solution containing MB and ZnO#10 significantly affects the photocatalytic process, promoting a reduction of the discoloration and photocatalytic reaction rates of the dye from 85% to 33% and 0.0153 $min^{-1}$ to 0.0033 $min^{-1}$ (Fig. 9(d)), respectively, which is ascribed to the low availability of free $HO^{\bullet}$ ions after their entrapment by IPA molecules. Similarly, the addition of BQ reduces the efficiency of the photocatalytic process to 40% due to the entrapment of $O_2^{\bullet -}$ anions by BQ molecules. Such results reveal that the interaction between visible light and ZnO#10 nanoparticles persistently produces $HO^{\bullet}$ and $O_2^{\bullet -}$ highly reactive chemical species that play a critical role in destructing MB organic molecules in an aqueous solution. Conversely, the holes do not influence the photocatalytic performance of ZnO#10 nanoparticles because adding the EDTA scavenger did not reduce dye degradation after 120 min irradiation with visible light.

Thus, the best photocatalytic activity dictated by the robust production of $HO^{\bullet}$ and $O_2^{\bullet -}$ chemical species under visible light was attributed to the ZnO#10 sample, which can be associated with its unique physical properties, e.g., shape, particle size, surface contaminations, and structural defects. Henceforth, all nanoparticles showed similar contamination on their surface; that is, $CO_2$ was not eliminated during the xerogel calcination, as shown in our FTIR analysis (Fig. 5), which cannot be attributed to the best photocatalytic performance found for ZnO#10. However, the morphological analysis revealed that our ZnO nanoparticles (Fig. 4) show small differences in particle size, where the smallest value was reported for Zn#10. The smaller particle size of Zn#10 combined with its higher surface area (30.7 $m^2.g^{-1}$) and pore volume (0.107 $cm^3.g^{-1}$) is also considered a key factor for the better photocatalytic performance of this sample. Furthermore, our

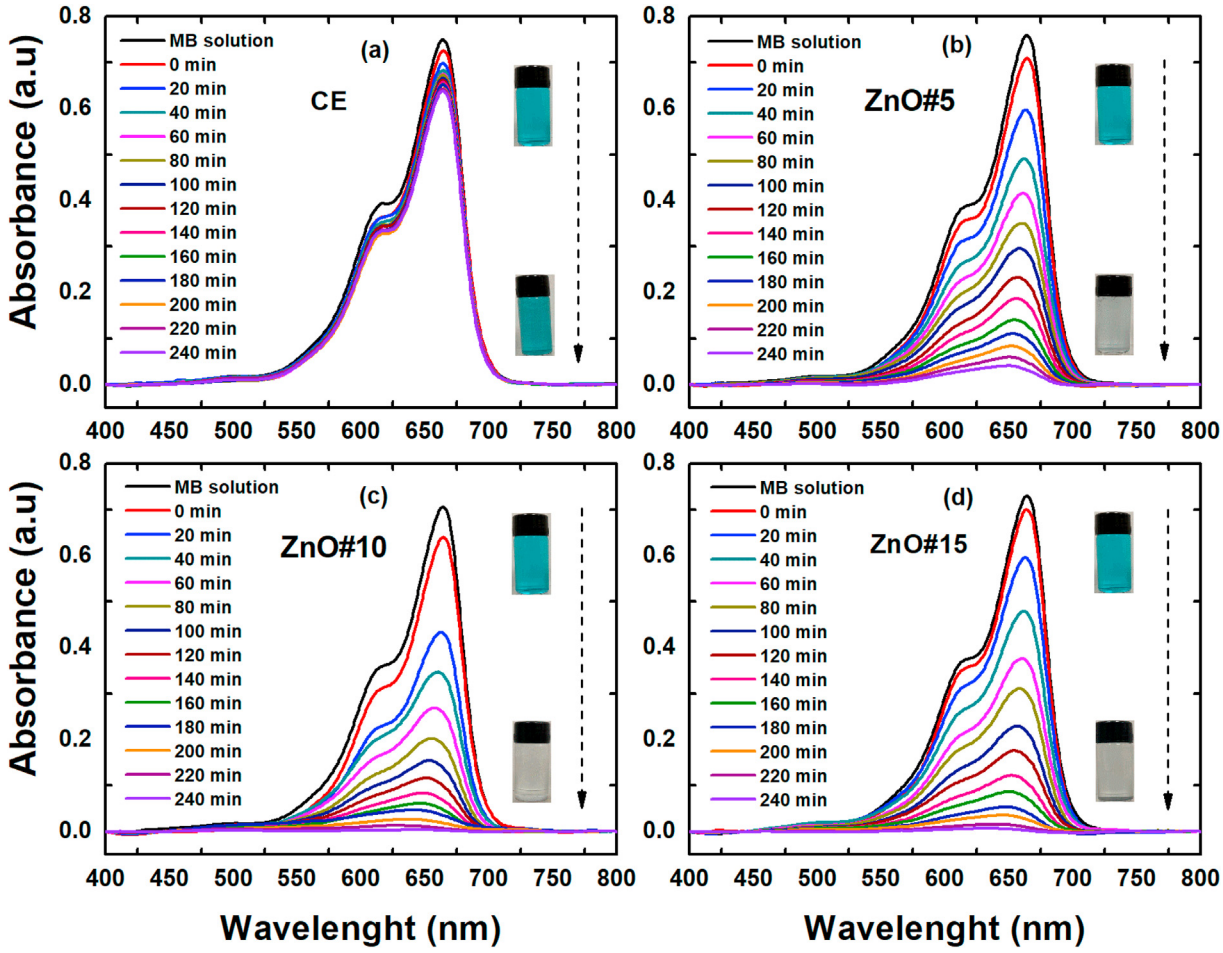


**Fig. 7 – UV–vis spectra of degradation of MB dye in aqueous solution (a) in the dark and containing (b) ZnO#5, (c) ZnO#10, and (d) ZnO#15 nanoparticles obtained for different irradiation times under visible light. The inserted scheme shows the evolution of dye discoloration after 240 min of irradiation.**

PL analysis revealed that only ZnO#10 has a bandgap tuned by the coexistence of $V_{Zn}$, $V_O^{++}$, $O_i^+$, and $Zn_O$ defects, whose origins can be comprehended as follows. The small atomic radius of $Zn^{2+}$ species allowed their diffusion to less oxidized chemical environments, i.e., $O^{2-}$ sites, creating both $V_{Zn}$ and $Zn_O$ defects. Concurrently, oxygen migrated to interstitial positions promoting the formation of $O_i$ and $V_O$, which further were single and doubly ionized, forming $O_i^+$ and $V_O^{++}$, respectively, releasing $e^-$ and $2e^-$ to the nanoparticles' surface. The greater ZnO#10 lattice compression (Table S1) also favored the bond between the oxygen present in interstitial positions and the Zn present in positions occupied initially by $O^{2-}$ ions generating its lower lattice axial ratio value (c/a = 1.598). This behavior stabilized the ZnO lattice and promoted an out-of-plane diffusion of the predominant defects by migrating them to the surface of the nanoparticles, where the grain boundary regions are considered as potential for agglomeration of these defects. Furthermore, according to Ferreira et al. [16], $V_{Zn}$ can create intermediate energy levels in the ZnO band gap so that electrons from VB need less energy to move to CB delaying the charge carrier's recombination. These results suggest a predominant presence of O-vacancies defects and the formation of defect levels other than O-vacancies within the band gap control the luminescence nature of ZnO#10. Thus, if we consider an O vacancy at the O1 site (2a), a local Zn1–O1 bond is expected to vanish, which would induce a Zn1 shift-up because of the empty O1 site above the Zn1 site. Consequently, the closer Zn2 atoms below the Zn1 site in the lattice structure likely induce two excessive electrons from Zn $4s^2$ orbital to experience upward Coulomb repulsion to increase the Fermi level concerning the valence band minimum, reaching a stable condition. This implies that charge transfer between Zn (4s)-O (2p) orbitals contributes to increasing charge carrier density, with oxygen vacancies containing two electrons $V_O^{++}$ acting as carrier donors. As a result, an excess electron is localized in the proximity of $V_{Zn}$, $V_O^{++}$, $O_i^+$, and $Zn_O$ defects, which attract holes from the ZnO valence band. However, lower carrier recombination on bulk ZnO nanoparticles promotes a higher transport of charge carriers, including separating photogenerated charge carriers, recombining easily at the surface of ZnO nanoparticles. Thus, the hole transfer from the bulk to the ZnO nanoparticle surface is most likely associated with potential band shift, indicating that the oxidation reaction of MB molecule on the ZnO

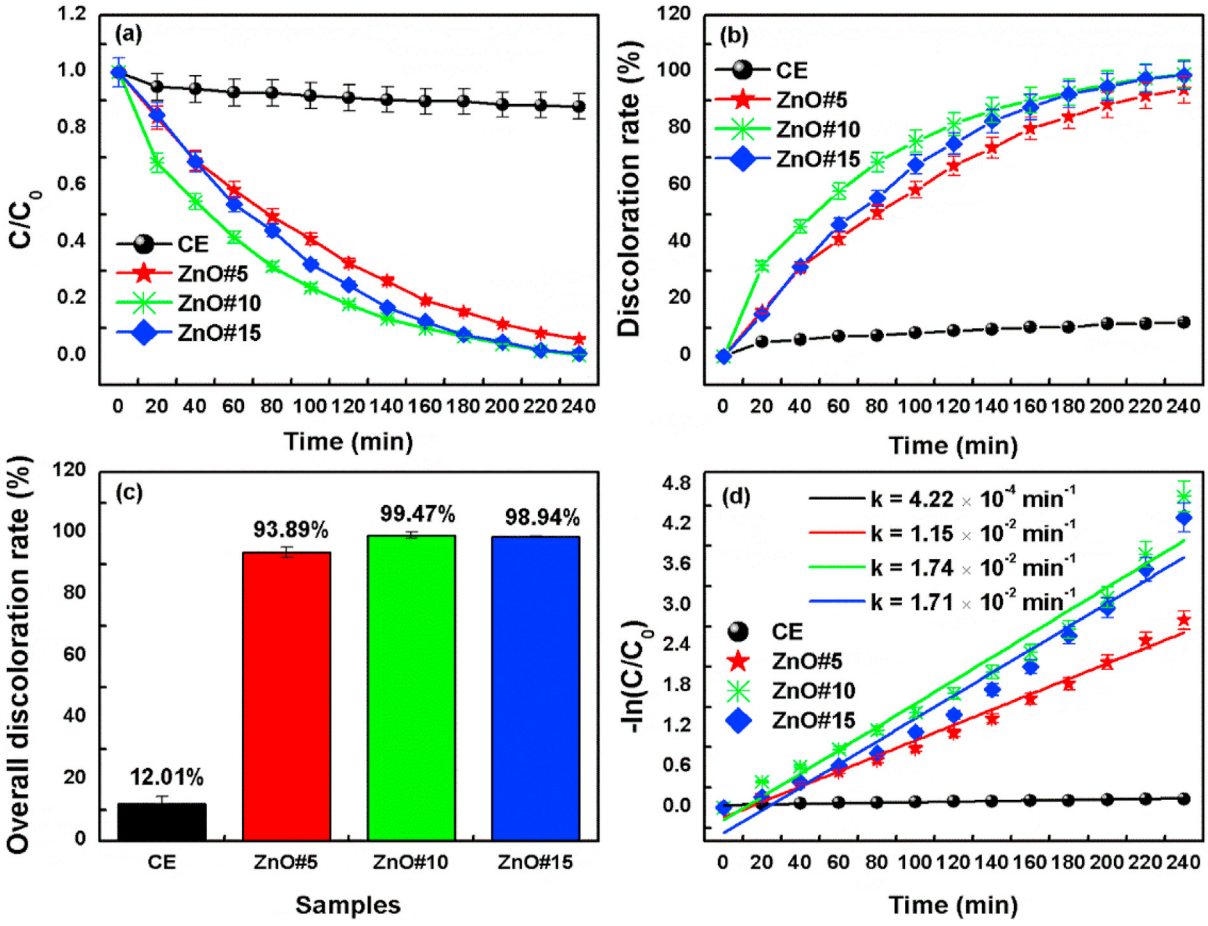


**Fig. 8 – (a) $C/C_0$ factor, (b) discoloration rate, (c) Overall discoloration rate, and (d) First-order kinetics of the degradation of MB dye in aqueous solutions containing ZnO nanoparticles non-irradiated and irradiated with visible light.**

nanoparticle surface is majorly from surface state holes instead of from valence band holes. Therefore, the possible mechanism of the ZnO#10 sample responsible for dictating its better MB dye discoloration under visible light is described as follows.

The probable mechanism responsible for the generation of highly reactive species that dictate the destruction of MB organic molecules by $HO^{\bullet}$ and $O_2^{\bullet-}$ chemical species is shown in Fig. 10. After irradiation with visible light, the electrons are excited up to $E_g \geq 3.02$ eV allowing the formation of the charge

**Table 2 – Comparative relationship between experimental parameters dye type (DT), photocatalyst weight (PW), dye concentration (DC), irradiation time (IT), light source (LS), and maximum photocatalytic efficiency (MPE) of ZnO nanoparticles with other photocatalysts.**

| Photocatalyst | DT | PW | DC | IT | LS | MPE | Reference |
|---|---|---|---|---|---|---|---|
| | – | mg | $mg.L^{-1}$ | min | – | % | – |
| ZnO | methylene blue | 10 | 10 | 240 | visible light | 99.47 | Present work |
| rGO-Gd@ZnO | rhodamine B | 50 | 10 | 40 | UV | 91 | [89] |
| F@g-C3N4/ZnO | rhodamine B | 50 | 10 | 75 | sunlight | 97 | [90] |
| Co–NiO | methylene blue | 100 | 10 | 120 | UV | 91 | [91] |
| ZnO/SCN | rhodamine B | 50 | 10 | 80 | visible light | 93 | [92] |
| Ni– ZnO | methylene blue | 50 | 10 | 240 | UV | 94 | [93] |
| 5% Gd-WO3 | rhodamine B | 5 | 20 | 100 | visible light | 94 | [94] |
| rGO/g-CN/CFO | 4-nitrophenol | 25 | 20 | 40 | visible light | 97 | [95] |
| 20NFO/SCNNR | tetracycline | 25 | 10 | 60 | visible light | 97 | [96] |
| g-C3N4/SnO2–Cu2O | methylene blue | 50 | 30 | 100 | visible light | 94.5 | [97] |
| g-C3N4/ZnO–Ag2O | methylene blue | 50 | 30 | 120 | visible light | 96.5 | [98] |
| 7%Li–ZnO | methylene green | 500 | 200 | 60 | visible light | 100 | [99] |
| CuO | methylene blue | 10 | 10 | 40 | visible light | 90 | [100] |

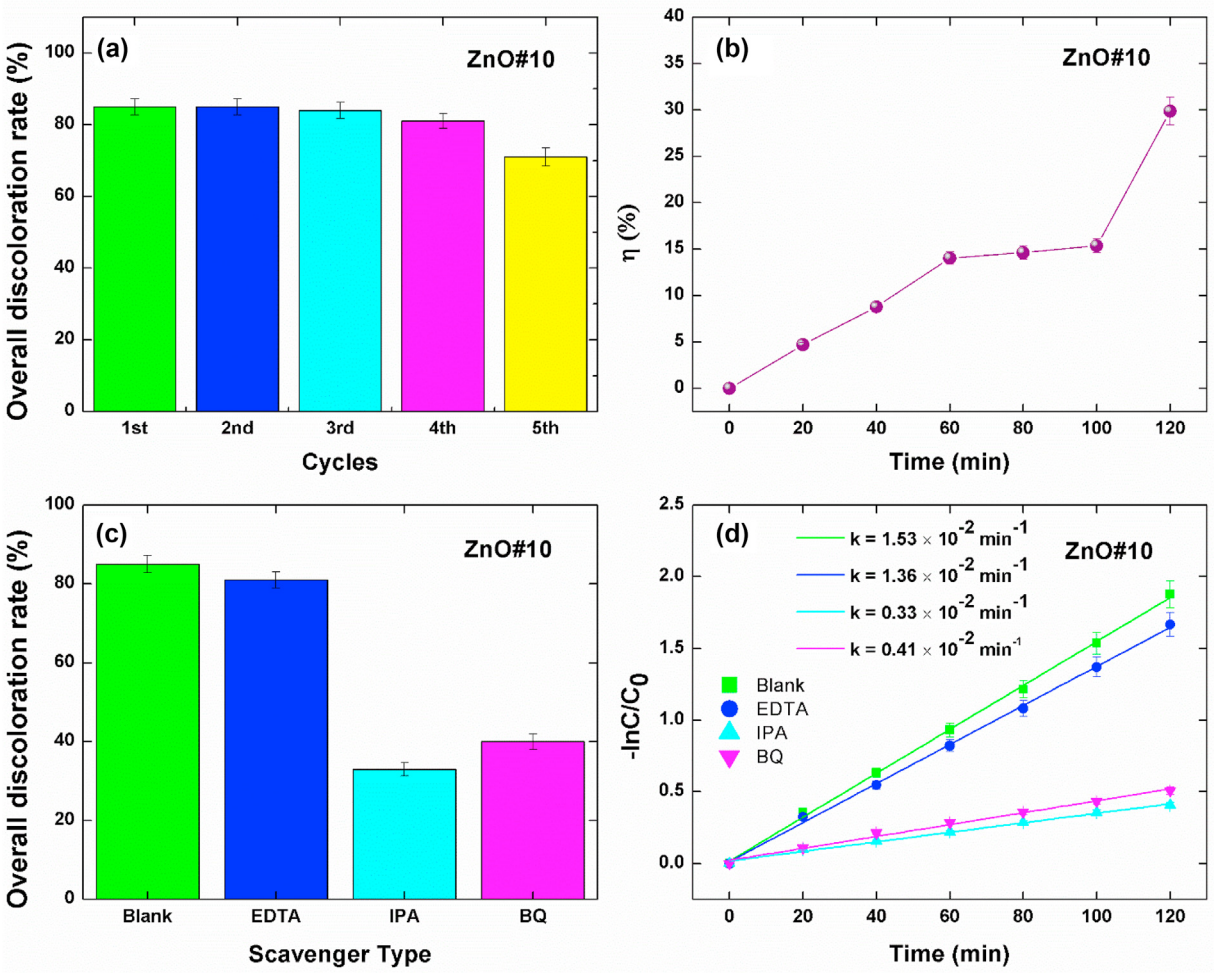


**Fig. 9 – (a) Overall discoloration rate of the photodegradation of MB dye under 5 cycles of reuse and (b) TOC removal efficiency of MB dye using ZnO#10 photocatalyst after the 5th cycle of the photodegradation. (c) Overall discoloration rate and (d) first-order kinetics plots obtained by the elemental trapping experiment.**

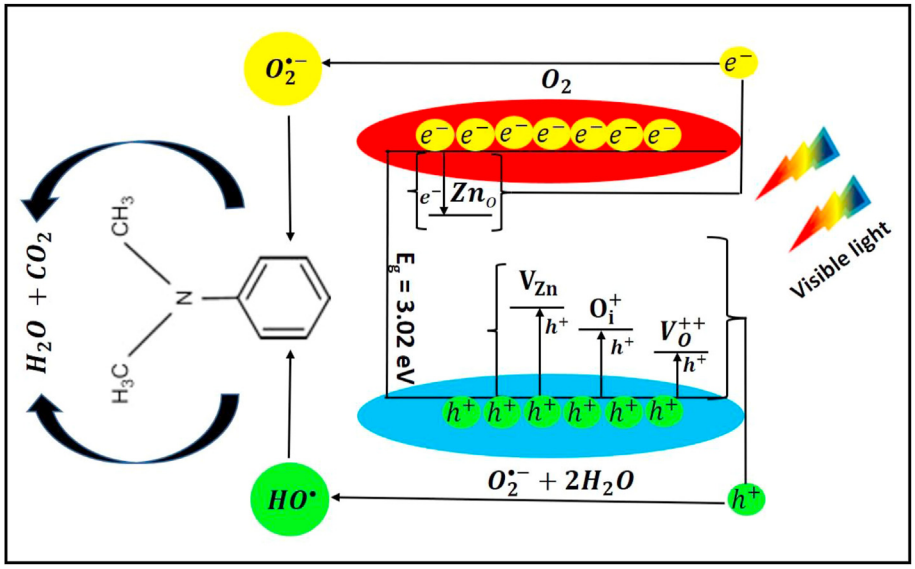


**Fig. 10 – The probable mechanism of the MB dye photodegradation using ZnO#10 nanoparticles as efficient photocatalysts.**

carriers ($e^-_{CB}/h^+_{VB}$) (Eq. (7)), which are transported to the surface of the nanoparticles, starting some redox reactions. On the surface, $e^-_{CB}$ and $h^+_{VB}$ interact with oxygen ($O_2$) and water ($H_2O$), forming superoxide ($O_2^{\bullet-}$) (Eq. (8)) and hydroxyl radical ($HO^\bullet$) (Eq. (9)), respectively. These reactions are responsible for the overall photodegradation mechanism of the MB molecules.

$$ZnO + \text{visible light} \rightarrow e^-_{CB} + h^+_{VB} \quad (7)$$

$$e^-_{CB} + O_2 \rightarrow O_2^{\bullet-} \quad (8)$$

$$h^+_{VB} + H_2O \rightarrow H^+ + HO^\bullet \quad (9)$$

However, the smaller particle size, large surface area, and the defects $V_{Zn}$, $V_O^{++}$, $O_i^+$, and $Zn_O$ present in ZnO#10 nanoparticles further enhances the photodegradation of MB dye. The large surface area and pore volume allow more significant adsorption of MB molecules on the surface of ZnO nanoparticles. After that, the $Zn_O$ defect traps photoexcited electrons, which are transferred to the surface of the nanoparticles and interact with $O_2$ to produce $O_2^{\bullet-}$ (Eq. (10)). Although the $h^+_{VB}$ present on the surface of the nanoparticles does not directly produce the degradation of the MB dye molecules, they are captured by $V_{Zn}$, $V_O^{++}$, and $O_i^+$ defects created in the optical bandgap, slowing down the recombination of charge carriers. Additionally, these holes interact with the $O_2^{\bullet-}$ anions to generate $HO^\bullet$ ions and hydrogen peroxide ($H_2O_2$) (Eq. (11)–(13)). The $H_2O_2$ can also be reduced into $HO^\bullet$ species by the visible light, as shown in Eq. (14). Finally, $O_2^{\bullet-}$ and $HO^\bullet$ chemical species attack the sulfhydryl ($R-S^+=R$) groups of MB dye producing several redox reactions that culminate in the formation of single molecules such as $H_2O$ and $CO_2$ [101,102].

$$\left(e^-_{Zn_O}\right) + O_2 \rightarrow \left(O_2^{\bullet-}\right) \quad (10)$$

$$h^+_{V_{Zn}} + O_2^{\bullet-} + 2H_2O \rightarrow 2HO^\bullet + H_2O_2 \quad (11)$$

$$h^+_{O_i^+} + O_2^{\bullet-} + 2H_2O \rightarrow 2HO^\bullet + H_2O_2 \quad (12)$$

$$h^+_{V_O^{++}} + O_2^{\bullet-} + 2H_2O \rightarrow 2HO^\bullet + H_2O_2 \quad (13)$$

$$H_2O_2 + \text{Visible Light} \rightarrow 2HO^\bullet \quad (14)$$

## 4. Conclusion

We have shown that the sweet Amapá-latex natural chelating agent arises as a sustainable and eco-friendly substance for synthesizing ZnO nanoparticles with defects-driven photocatalytic performance. XRD and FTIR analyses confirmed the formation of the ZnO nanoparticles with a wurtzite-like structure and crystallite size ranging from 13.5 to 16.4 nm, formed by chelating of $Zn^{2+}$ ions by pentacyclic triterpenes present in the sweet Amapá-latex chelating agent structure. TEM analysis showed that the ZnO nanoparticles have polycrystalline nature and particle size of 14.1–16.5 nm, in good agreement with XRD analyses. Our PL analysis showed that the optical bandgap of 3.02 eV of the sample ZnO#10 was tunned by the coexistence of $V_{Zn}$, $V_O^{++}$, $O_i^+$, and $Zn_O$ structural defects. Finally, the photocatalytic experiment showed that the best degradation rate of the MB dye in an aqueous solution is 99.47% after 240 min of irradiation with visible light was assigned to the ZnO#10 sample. Such behavior was ascribed to the small particle size, high surface area, and unique defective structure of ZnO#10, which dictated the substantial production of hydroxyl radicals that led to the destruction of MB dye organic molecules. Furthermore, the cyclic photodegradation experiment proved that ZnO#10 sample can be used for 5 degradation cycles without significant loss of photocatalytic performance. Therefore, these findings reveal that the defective structure of ZnO nanoparticles can be controlled by the contents of sweet Amapa-latex used for the synthesis, directly influencing the production of chemical species that can attack and destroy organic dye molecules.

## Declaration of competing interest

The authors declare that they have no known competing financial interests or personal relationships that could have appeared to influence the work reported in this paper.

## Appendix A. Supplementary data

Supplementary data to this article can be found online at https://doi.org/10.1016/j.jmrt.2022.12.119.

## REFERENCES

[1] Verma R, Pathak S, Srivastava AK, Prawer S, Tomljenovic-Hanic S. ZnO nanomaterials: green synthesis, toxicity evaluation and new insights in biomedical applications. J Alloys Compd 2021;876:160175. https://doi.org/10.1016/j.jallcom.2021.160175.

[2] Gonçalves RA, Toledo RP, Joshi N, Berengue OM. Green synthesis and applications of ZnO and TiO2 nanostructures. Molecules 2021;26:2236. https://doi.org/10.3390/molecules26082236.

[3] Shashanka R, Esgin H, Yilmaz VM, Caglar Y. Fabrication and characterization of green synthesized ZnO nanoparticle based dye-sensitized solar cells. J. Sci. Adv. Mater. Devices. 2020;5:185–91. https://doi.org/10.1016/j.jsamd.2020.04.005.

[4] Rajendrachari S, Taslimi P, Karaoglanli AC, Uzun O, Alp E, Jayaprakash GK. Photocatalytic degradation of Rhodamine B (RhB) dye in waste water and enzymatic inhibition study using cauliflower shaped ZnO nanoparticles synthesized by a novel One-pot green synthesis method. Arab J Chem 2021;14:103180. https://doi.org/10.1016/j.arabjc.2021.103180.

[5] Yadav R, Chundawat TS, Rawat P, Rao GK, Vaya D. Photocatalytic degradation of malachite green dye by ZnO and ZnO–β-cyclodextrin nanocomposite. Bull Mater Sci 2021;44:250. https://doi.org/10.1007/s12034-021-02533-z.

[6] Habibi A, Vatandoust L, Aref SM, Naghshara H. Formation of high performance nanostructured ZnO thin films as a function of annealing temperature: structural and optical properties. Surface Interfac 2020;21:100723. https://doi.org/10.1016/j.surfin.2020.100723.

[7] van Dijken A, Meulenkamp EA, Vanmaekelbergh D, Meijerink A. Identification of the transition responsible for the visible emission in ZnO using quantum size effects. J Lumin 2000;90:123–8. https://doi.org/10.1016/S0022-2313(99)00599-2.
[8] Gouveia Guedes CE, de Oliveira DNPS, Bezerra JB, de Oliveira Penido CAF, Ferreira NS, Lustrino Borges W, et al. Exploiting the amazonian açaí palm leaves potential as reinforcement for cement composites through alkali and bleaching treatments. J Nat Fibers 2021:1–14. https://doi.org/10.1080/15440478.2021.1941483.
[9] Shekofteh-Gohari M, Habibi-Yangjeh A, Abitorabi M, Rouhi A. Magnetically separable nanocomposites based on ZnO and their applications in photocatalytic processes: a review. Crit Rev Environ Sci Technol 2018;48:806–57. https://doi.org/10.1080/10643389.2018.1487227.
[10] Mohammadzadeh A, Khoshghadam-Pireyousefan M, Shokrianfard-Ravasjan B, Azadbeh M, Rashedi H, Dibazar M, et al. Synergetic photocatalytic effect of high purity ZnO pod shaped nanostructures with H2O2 on methylene blue dye degradation. J Alloys Compd 2020;845:156333. https://doi.org/10.1016/j.jallcom.2020.156333.
[11] Aldeen TS, Ahmed Mohamed HE, Maaza M. ZnO nanoparticles prepared via a green synthesis approach: physical properties, photocatalytic and antibacterial activity. J Phys Chem Solid 2022;160:110313. https://doi.org/10.1016/j.jpcs.2021.110313.
[12] Wang L, Li Z, Chen J, Huang Y, Zhang H, Qiu H. Enhanced photocatalytic degradation of methyl orange by porous graphene/ZnO nanocomposite. Environ Pollut 2019;249:801–11. https://doi.org/10.1016/j.envpol.2019.03.071.
[13] Jayakrishnan C, Sheeja SR, Duraimurugan J, Prabhu S, Ramesh R, Kumar GS, et al. Photoelectrochemical properties and photocatalytic degradation of methyl orange dye by different ZnO nanostructures. J Mater Sci Mater Electron 2022;33:9732–42. https://doi.org/10.1007/s10854-022-07801-0.
[14] Nandi P, Das D. Photocatalytic degradation of Rhodamine-B dye by stable ZnO nanostructures with different calcination temperature induced defects. Appl Surf Sci 2019;465:546–56. https://doi.org/10.1016/j.apsusc.2018.09.193.
[15] Bharathi D, AlSalhi MS, Devanesan S, Nandagopal JGT, Kim W, Ranjithkumar R. Photocatalytic degradation of Rhodamine B using green-synthesized ZnO nanoparticles from Sechium edule polysaccharides. Appl Nanosci 2022;12:2477–87. https://doi.org/10.1007/s13204-022-02502-w.
[16] Ferreira NS, Sasaki JM, Silva RS, Attah-Baah JM, Macêdo MA. Visible-light-responsive photocatalytic activity significantly enhanced by active [ V Zn + V O + ] defects in self-assembled ZnO nanoparticles. Inorg Chem 2021;60:4475–96. https://doi.org/10.1021/acs.inorgchem.0c03327.
[17] Matos RS, Attah-Baah JM, Monteiro MDS, Costa BFO, Mâcedo MA, Da Paz SPA, et al. Evaluation of the photocatalytic activity of distinctive-shaped ZnO nanocrystals synthesized using latex of different plants native to the Amazon rainforest. Nanomaterials 2022;12:2889. https://doi.org/10.3390/nano12162889.
[18] Amjad M, Khan MI, Alwadai N, Irfan M, Ikram-ul-Haq, Albalawi H, et al. Photovoltaic properties of ZnO films Co-doped with Mn and La to enhance solar cell efficiency. Nanomaterials 2022;12:1057. https://doi.org/10.3390/nano12071057.
[19] Ahmed S, Chaudhry SA, Ikram S. A review on biogenic synthesis of ZnO nanoparticles using plant extracts and microbes: a prospect towards green chemistry. J Photochem Photobiol B Biol 2017;166:272–84. https://doi.org/10.1016/j.jphotobiol.2016.12.011.
[20] Ahmed S, Ahmad M, Swami BL, Ikram S. A review on plants extract mediated synthesis of silver nanoparticles for antimicrobial applications: a green expertise. J Adv Res 2016;7:17–28. https://doi.org/10.1016/j.jare.2015.02.007.
[21] Vijayan SR, Santhiyagu P, Ramasamy R, Arivalagan P, Kumar G, Ethiraj K, et al. Seaweeds: a resource for marine bionanotechnology. Enzym Microb Technol 2016;95:45–57. https://doi.org/10.1016/j.enzmictec.2016.06.009.
[22] de Lima BR, da Silva FMA, Soares ER, de Almeida RA, da Silva-Filho FA, Barison A, et al. Integrative approach based on leaf spray mass spectrometry, HPLC-DAD-MS/MS, and NMR for comprehensive characterization of isoquinoline-derived alkaloids in leaves of Onychopetalum amazonicum R. E Fr J Braz Chem Soc. 2020;31:79–89. https://doi.org/10.21577/0103-5053.20190125.
[23] Lopes de Almeida W, Ferreira NS, Rodembusch FS, Caldas de Sousa V. Study of structural and optical properties of ZnO nanoparticles synthesized by an eco-friendly tapioca-assisted route. Mater Chem Phys 2020:123926. https://doi.org/10.1016/j.matchemphys.2020.123926.
[24] Rodríguez-Carvajal J. Recent advances in magnetic structure determination by neutron powder diffraction. Phys B Condens Matter 1993;192:55–69. https://doi.org/10.1016/0921-4526(93)90108-I.
[25] Matos RS, Monteiro MDS, Silva RS, Macêdo MA, Paz SPA, Angélica RS, et al. Novel Amapá latex-mediated synthesis of defective α-Fe2O3 nanoparticles with enhanced ferromagnetism and sunlight photocatalytic activity. Ceram Int 2022. https://doi.org/10.1016/j.ceramint.2022.06.164.
[26] Suresh S, Karthikeyan S, Jayamoorthy K. Spectral investigations to the effect of bulk and nano ZnO on peanut plant leaves. Karbala Int J Mod Sci 2016;2:69–77. https://doi.org/10.1016/j.kijoms.2016.01.005.
[27] Hales MC, Frost RL. Synthesis and vibrational spectroscopic characterisation of synthetic hydrozincite and smithsonite. Polyhedron 2007;26:4955–62. https://doi.org/10.1016/j.poly.2007.07.002.
[28] Santhoshkumar J, Kumar SV, Rajeshkumar S. Synthesis of zinc oxide nanoparticles using plant leaf extract against urinary tract infection pathogen. Resour Technol 2017;3:459–65. https://doi.org/10.1016/j.reffit.2017.05.001.
[29] Nassar MY, Moustafa MM, Taha MM. Hydrothermal tuning of the morphology and particle size of hydrozincite nanoparticles using different counterions to produce nanosized ZnO as an efficient adsorbent for textile dye removal. RSC Adv 2016;6:42180–95. https://doi.org/10.1039/C6RA04855B.
[30] Quy CT, Hung CM, Van Duy N, Hoa ND, Jiao M, Nguyen H. Ethanol-sensing characteristics of nanostructured ZnO: nanorods, nanowires, and porous nanoparticles. J Electron Mater 2017;46:3406–11. https://doi.org/10.1007/s11664-016-5270-2.
[31] Sahai A, Goswami N. Structural and vibrational properties of ZnO nanoparticles synthesized by the chemical precipitation method. Phys E Low-Dimensional Syst Nanostructures. 2014;58:130–7. https://doi.org/10.1016/j.physe.2013.12.009.
[32] Kumar S, Asokan K, Singh RK, Chatterjee S, Kanjilal D, Ghosh AK. Investigations on structural and optical properties of ZnO and ZnO:Co nanoparticles under dense electronic excitations. RSC Adv 2014;4:62123–31. https://doi.org/10.1039/C4RA09937K.
[33] Jayappa MD, Ramaiah CK, Kumar MAP, Suresh D, Prabhu A, Devasya RP, et al. Green synthesis of zinc oxide nanoparticles from the leaf, stem and in vitro grown callus

of Mussaenda frondosa L.: characterization and their applications. Appl Nanosci 2020;10:3057–74. https://doi.org/10.1007/s13204-020-01382-2.
[34] Roopan SM, Mathew RS, Mahesh SS, Titus D, Aggarwal K, Bhatia N, et al. Environmental friendly synthesis of zinc oxide nanoparticles and estimation of its larvicidal activity against Aedes aegypti. Int J Environ Sci Technol 2019;16:8053–60. https://doi.org/10.1007/s13762-018-2175-z.
[35] Arathi A, Joseph X, Akhil V, Mohanan P. L-Cysteine capped zinc oxide nanoparticles induced cellular response on adenocarcinomic human alveolar basal epithelial cells using a conventional and organ-on-a-chip approach. Colloids Surf, B 2022;211:112300. https://doi.org/10.1016/j.colsurfb.2021.112300.
[36] Barzinjy AA, Abdul DA, Hussain FHS, Hamad SM. Green synthesis of the magnetite (Fe 3 O 4)nanoparticle using Rhus coriaria extract: a reusable catalyst for efficient synthesis of some new 2-naphthol bis-Betti bases. Inorg. Nano-Metal Chem. 2020;50:620–9. https://doi.org/10.1080/24701556.2020.1723027.
[37] Varadavenkatesan T, Lyubchik E, Pai S, Pugazhendhi A, Vinayagam R, Selvaraj R. Photocatalytic degradation of Rhodamine B by zinc oxide nanoparticles synthesized using the leaf extract of Cyanometra ramiflora. J Photochem Photobiol B Biol 2019;199:111621. https://doi.org/10.1016/j.jphotobiol.2019.111621.
[38] Pai S, H S, Varadavenkatesan T, Vinayagam R, Selvaraj R. Photocatalytic zinc oxide nanoparticles synthesis using Peltophorum pterocarpum leaf extract and their characterization. Optik 2019;185:248–55. https://doi.org/10.1016/j.ijleo.2019.03.101.
[39] Molaei P, Rahimi Moghadam F. Seed-free synthesis of ZnO nanorods through egg white/glycerol medium for photocatalyst applications. Mater Today Commun 2022;31:103677. https://doi.org/10.1016/j.mtcomm.2022.103677.
[40] Zargar RA, Arora M, Bhat RA. Study of nanosized copper-doped ZnO dilute magnetic semiconductor thick films for spintronic device applications. Appl Phys A 2018;124:36. https://doi.org/10.1007/s00339-017-1457-5.
[41] Talam S, Karumuri SR, Gunnam N. Synthesis, characterization, and spectroscopic properties of ZnO nanoparticles. ISRN Nanotechnol 2012;(2012):1–6. https://doi.org/10.5402/2012/372505.
[42] Soares VA, Xavier MJS, Rodrigues ES, de Oliveira CA, Farias PMA, Stingl A, et al. Green synthesis of ZnO nanoparticles using whey as an effective chelating agent. Mater Lett 2020;259:126853. https://doi.org/10.1016/j.matlet.2019.126853.
[43] Wu L, Wu Y, Pan X, Kong F. Synthesis of ZnO nanorod and the annealing effect on its photoluminescence property. Opt Mater 2006;28:418–22. https://doi.org/10.1016/j.optmat.2005.03.007.
[44] Cho S, Ma J, Kim Y, Sun Y, Wong GKL, Ketterson JB. Photoluminescence and ultraviolet lasing of polycrystalline ZnO thin films prepared by the oxidation of the metallic Zn. Appl Phys Lett 1999;75:2761–3. https://doi.org/10.1063/1.125141.
[45] Aljawfi RN, Alam MJ, Rahman F, Ahmad S, Shahee A, Kumar S. Impact of annealing on the structural and optical properties of ZnO nanoparticles and tracing the formation of clusters via DFT calculation. Arab J Chem 2020;13:2207–18. https://doi.org/10.1016/j.arabjc.2018.04.006.
[46] Shao HP, Tan YM, Lin T, Guo ZM. Size-controlled synthesis of magnetite nanoparticles from iron acetate by thermal decomposition. Appl Mech Mater 2012;217–219:256–9. https://doi.org/10.4028/www.scientific.net/AMM.217-219.256.
[47] Ahn CH, Kim YY, Kim DC, Mohanta SK, Cho HK. A comparative analysis of deep level emission in ZnO layers deposited by various methods. J Appl Phys 2009;105:013502. https://doi.org/10.1063/1.3054175.
[48] Zhang YZ, Lu JG, Ye ZZ, He HP, Zhu LP, Zhao BH, et al. Effects of growth temperature on Li–N dual-doped p-type ZnO thin films prepared by pulsed laser deposition. Appl Surf Sci 2008;254:1993–6. https://doi.org/10.1016/j.apsusc.2007.08.008.
[49] Ashokkumar M, Muthukumaran S. Effect of Ni doping on electrical, photoluminescence and magnetic behavior of Cu doped ZnO nanoparticles. J Lumin 2015;162:97–103. https://doi.org/10.1016/j.jlumin.2015.02.019.
[50] Tummapudi N, Modem S, Jaladi NK, Choudary G, Kurapati SR. Structural, morphological, optical and mechanical studies of annealed ZnO nano particles. Phys B Condens Matter 2020;597:412401. https://doi.org/10.1016/j.physb.2020.412401.
[51] Sun Q, Wang H, Yang C, Li Y. Synthesis and electroluminescence of novel copolymers containing crown ether spacers. J Mater Chem 2003;13:800–6. https://doi.org/10.1039/b209469j.
[52] Haja Hameed AS, Louis G, Karthikeyan C, Thajuddin N, Ravi G. Impact of l-Arginine and l-Histidine on the structural, optical and antibacterial properties of Mg doped ZnO nanoparticles tested against extended-spectrum beta-lactamases (ESBLs) producing Escherichia coli. Spectrochim Acta Part A Mol Biomol Spectrosc 2019;211:373–82. https://doi.org/10.1016/j.saa.2018.12.025.
[53] Hameed ASH, Karthikeyan C, Ahamed AP, Thajuddin N, Alharbi NS, Alharbi SA, et al. In vitro antibacterial activity of ZnO and Nd doped ZnO nanoparticles against ESBL producing Escherichia coli and Klebsiella pneumoniae. Sci Rep 2016;6:24312. https://doi.org/10.1038/srep24312.
[54] Gandhi V, Ganesan R, Abdulrahman Syedahamed HH, Thaiyan M. Effect of cobalt doping on structural, optical, and magnetic properties of ZnO nanoparticles synthesized by coprecipitation method. J Phys Chem C 2014;118:9715–25. https://doi.org/10.1021/jp411848t.
[55] Peng-Shou X, Yu-Ming S, Chao-Shu S, Fa-Qiang X, Hai-Bin P. Native point defect states in ZnO. Chin Phys Lett 2001;18:1252–3. https://doi.org/10.1088/0256-307X/18/9/331.
[56] Fang M, Tang CM, Liu ZW. Microwave-Assisted hydrothermal synthesis of Cu-doped ZnO single crystal nanoparticles with modified photoluminescence and confirmed ferromagnetism. J Electron Mater 2018;47:1390–6. https://doi.org/10.1007/s11664-017-5928-4.
[57] Mariappan R, Ponnuswamy V, Suresh P. Effect of doping concentration on the structural and optical properties of pure and tin doped zinc oxide thin films by nebulizer spray pyrolysis (NSP) technique. Superlattice Microst 2012;52:500–13. https://doi.org/10.1016/j.spmi.2012.05.016.
[58] Ravichandran AT, Karthick R. Enhanced photoluminescence, structural, morphological and antimicrobial efficacy of Co-doped ZnO nanoparticles prepared by Co-precipitation method. Results Mater 2020;5:100072. https://doi.org/10.1016/j.rinma.2020.100072.
[59] Arunpandian M, Marnadu R, Kannan R, Karthik Kannan S, Johnsy Arputhavalli G, Ignatius Arockiam S, et al. Fabrication of Cu/ZnO system: a dual performer as photocatalyst and luminescent material. Inorg Chem Commun 2021;134:109022. https://doi.org/10.1016/j.inoche.2021.109022.
[60] Karthika K, Ravichandran K. Tuning the microstructural and magnetic properties of ZnO nanopowders through the simultaneous doping of Mn and Ni for biomedical

applications. J Mater Sci Technol 2015;31:1111–7. https://doi.org/10.1016/j.jmst.2015.09.001.
[61] Monticone S, Tufeu R, Kanaev AV. Complex nature of the UV and visible fluorescence of colloidal ZnO nanoparticles. J Phys Chem B 1998;102:2854–62. https://doi.org/10.1021/jp973425p.
[62] Dutta M, Basak D. A novel and simple method to grow beaded nanochains of ZnO with superior photocatalytic activity. Nanotechnology 2009;20:475602. https://doi.org/10.1088/0957-4484/20/47/475602.
[63] Bharti DB, Bharati AV. Synthesis of ZnO nanoparticles using a hydrothermal method and a study its optical activity. Luminescence 2017;32:317–20. https://doi.org/10.1002/bio.3180.
[64] Sharma D, Jha R. Transition metal (Co, Mn) co-doped ZnO nanoparticles: effect on structural and optical properties. J Alloys Compd 2017;698:532–8. https://doi.org/10.1016/j.jallcom.2016.12.227.
[65] Othman AA, Ali MA, Ibrahim EMM, Osman MA. Influence of Cu doping on structural, morphological, photoluminescence, and electrical properties of ZnO nanostructures synthesized by ice-bath assisted sonochemical method. J Alloys Compd 2016;683:399–411. https://doi.org/10.1016/j.jallcom.2016.05.131.
[66] Pal B, Sarkar D, Giri PK. Structural, optical, and magnetic properties of Ni doped ZnO nanoparticles: correlation of magnetic moment with defect density. Appl Surf Sci 2015;356:804–11. https://doi.org/10.1016/j.apsusc.2015.08.163.
[67] Othman AA, Osman MA, Ibrahim EMM, Ali MA. Sonochemically synthesized ZnO nanosheets and nanorods: annealing temperature effects on the structure, and optical properties. Ceram Int 2017;43:527–33. https://doi.org/10.1016/j.ceramint.2016.09.189.
[68] Hamzah M, Ndimba RM, Khenfouch M, Srinivasu VV. Blue luminescence from hydrothermal ZnO nanorods based PVA nanofibers. J Mater Sci Mater Electron 2017;28:11915–20. https://doi.org/10.1007/s10854-017-7000-9.
[69] Periyayya U, Kang JH, Ryu JH, Hong C-H. Synthesis and improved luminescence properties of OLED/ZnO hybrid materials. Vacuum 2011;86:254–60. https://doi.org/10.1016/j.vacuum.2011.06.016.
[70] Kumar S, Sahare PD. Effects of annealing on the surface defects of zinc oxide nanoparticles. Nano 2012;7:1250022. https://doi.org/10.1142/S1793292012500221.
[71] Hantour H, Mohsen N, El-Sayed S, Mahmoud A. Luminescence investigation of powder zno nanoparticles doped with sm and li ions prepared by coprecipitation method. Al-Azhar Bull. Sci. 2017;28:27–33. https://doi.org/10.21608/absb.2017.8175.
[72] Gaur LK, Gairola P, Gairola SP, Mathpal MC, Kumar P, Kumar S, et al. Cobalt doping induced shape transformation and its effect on luminescence in zinc oxide rod-like nanostructures. J Alloys Compd 2021;868:159189. https://doi.org/10.1016/j.jallcom.2021.159189.
[73] Rana SB, Singh A, Kaur N. Structural and optoelectronic characterization of prepared and Sb doped ZnO nanoparticles. J Mater Sci Mater Electron 2013;24:44–52. https://doi.org/10.1007/s10854-012-0795-5.
[74] Rana SB, Bhardwaj VK, Singh S, Singh A, Kaur N. Influence of surface modification by 2-aminothiophenol on optoelectronics properties of ZnO nanoparticles. J Exp Nanosci 2014;9:877–91. https://doi.org/10.1080/17458080.2012.736640.
[75] Chen C, Liu X, Fang Q, Chen X, Liu T, Zhang M. Self-assembly synthesis of CuO/ZnO hollow microspheres and their photocatalytic performance under natural sunlight. Vacuum 2020;174:109198. https://doi.org/10.1016/j.vacuum.2020.109198.
[76] Boukhoubza I, Khenfouch M, Achehboune M, Mothudi BM, Zorkani I, Jorio A. Graphene oxide/ZnO nanorods/graphene oxide sandwich structure: the origins and mechanisms of photoluminescence. J Alloys Compd 2019;797:1320–6. https://doi.org/10.1016/j.jallcom.2019.04.266.
[77] Mahajan P, Singh A, Arya S. Improved performance of solution processed organic solar cells with an additive layer of sol-gel synthesized ZnO/CuO core/shell nanoparticles. J Alloys Compd 2020;814:152292. https://doi.org/10.1016/j.jallcom.2019.152292.
[78] Samavati A, Awang A, Samavati Z, Fauzi Ismail A, Othman MHD, Velashjerdi M, et al. Influence of ZnO nanostructure configuration on tailoring the optical bandgap: theory and experiment. Mater Sci Eng B 2021;263:114811. https://doi.org/10.1016/j.mseb.2020.114811.
[79] Zhao S, Cai H, Li P. Pure purple line and red line emissions of ZnO nanomaterials. J Nanosci Nanotechnol 2016;16:7738–41. https://doi.org/10.1166/jnn.2016.13065.
[80] Ghamsari MS, Alamdari S, Razzaghi D, Arshadi Pirlar M. ZnO nanocrystals with narrow-band blue emission. J Lumin 2019;205:508–18. https://doi.org/10.1016/j.jlumin.2018.09.064.
[81] Sawada K, Shirotori Y, Ozawa K, Edamoto K, Nakatake M. Valence band structure of the ZnO (1010) surface studied by angle-resolved photoemission spectroscopy. Appl Surf Sci 2004;237:343–7. https://doi.org/10.1016/j.apsusc.2004.06.100.
[82] Raoufi D. Synthesis and photoluminescence characterization of ZnO nanoparticles. J Lumin 2013;134:213–9. https://doi.org/10.1016/j.jlumin.2012.08.045.
[83] Shivakumara C, John AK, Behera S, Dhananjaya N, Saraf R. Photoluminescence and photocatalytic properties of Eu3+-doped ZnO nanoparticles synthesized by the nitrate-citrate gel combustion method. Eur. Phys. J. Plus. 2017;132:44. https://doi.org/10.1140/epjp/i2017-11304-5.
[84] Xuan Sang N, Minh Quan N, Huu Tho N, Tri Tuan N, Thanh Tung T. Mechanism of enhanced photocatalytic activity of Cr-doped ZnO nanoparticles revealed by photoluminescence emission and electron spin resonance. Semicond Sci Technol 2019;34:025013. https://doi.org/10.1088/1361-6641/aaf820.
[85] Sowri Babu K, Ramachandra Reddy A, Sujatha C, Venugopal Reddy K. Optimization of UV emission intensity of ZnO nanoparticles by changing the excitation wavelength. Mater Lett 2013;99:97–100. https://doi.org/10.1016/j.matlet.2013.02.079.
[86] Lv J, Li C, Chai Z. Defect luminescence and its mediated physical properties in ZnO. J Lumin 2019;208:225–37. https://doi.org/10.1016/j.jlumin.2018.12.050.
[87] Patwari G, Bodo BJ, Singha R, Kalita PK. Photoluminescence studies of H2O2 treated chemically synthesized ZnO nanostructures. Res J Chem Sci 2013;3:45–50. www.isca.in. [Accessed 12 November 2021]. accessed.
[88] Wang J, Gao L. Hydrothermal synthesis and photoluminescence properties of ZnO nanowires. Solid State Commun 2004;132:269–71. https://doi.org/10.1016/j.ssc.2004.07.052.
[89] Palanivel B, Hossain MS, Macadangdang RR, Sahaya Jude Dhas S, Al-Enizi AM, Ubaidullah M, et al. Effect of rGO support on Gd@ZnO for UV–visible-light driven photocatalytic organic pollutant degradation. J Rare Earths 2022. https://doi.org/10.1016/j.jre.2022.07.019.
[90] Kalisamy P, Shahadat Hossain M, Macadangdang RR, Madhubala V, Palanivel B, Venkatachalam M, et al. ZnO coupled F-doped g-C3N4: Z-scheme heterojunction for

visible-light driven photocatalytic degradation reaction. Inorg Chem Commun 2022;135:109102. https://doi.org/10.1016/j.inoche.2021.109102.
[91] Shkir M, Palanivel B, Khan A, Ahmad N, Mani A. Tailoring the structural, optical and remarkably enhanced photocatalytic activities of nickel oxide nanostructures through cobalt doping. Surface Interfac 2021;27:101515. https://doi.org/10.1016/j.surfin.2021.101515.
[92] Kalisamy P, Lallimathi M, Suryamathi M, Palanivel B, Venkatachalam M. ZnO-embedded S-doped g-C 3 N 4 heterojunction: mediator-free Z-scheme mechanism for enhanced charge separation and photocatalytic degradation. RSC Adv 2020;10:28365–75. https://doi.org/10.1039/D0RA04642F.
[93] Shkir M, Palanivel B, Khan A, Kumar M, Chang J-H, Mani A, et al. Enhanced photocatalytic activities of facile auto-combustion synthesized ZnO nanoparticles for wastewater treatment: an impact of Ni doping. Chemosphere 2022;291:132687. https://doi.org/10.1016/j.chemosphere.2021.132687.
[94] Govindaraj T, Mahendran C, Marnadu R, Shkir M, Manikandan VS. The remarkably enhanced visible-light-photocatalytic activity of hydrothermally synthesized WO3 nanorods: an effect of Gd doping. Ceram Int 2021;47:4267–78. https://doi.org/10.1016/j.ceramint.2020.10.004.
[95] Palanivel B, Lallimathi M, Arjunkumar B, Shkir M, Alshahrani T, Al-Namshah KS, et al. rGO supported g-C3N4/CoFe2O4 heterojunction: visible-light-active photocatalyst for effective utilization of H2O2 to organic pollutant degradation and OH radicals production. J Environ Chem Eng 2021;9:104698. https://doi.org/10.1016/j.jece.2020.104698.
[96] Palanivel B, Shkir M, Alshahrani T, Mani A. Novel NiFe2O4 deposited S-doped g-C3N4 nanorod: visible-light-driven heterojunction for photo-Fenton like tetracycline degradation. Diam Relat Mater 2021;112:108148. https://doi.org/10.1016/j.diamond.2020.108148.
[97] Vignesh S, Palanisamy G, Srinivasan M, Elavarasan N, Bhuvaneswari K, Venkatesh G, et al. Fabricating SnO2 and Cu2O anchored on g-C3N4 nanocomposites for superior photocatalytic various organic pollutants degradation under simulated sunlight exposure. Diam Relat Mater 2021;120:108606. https://doi.org/10.1016/j.diamond.2021.108606.
[98] Vignesh S, Eniya P, Srinivasan M, Kalyana Sundar J, Li H, Jayavel S, et al. Fabrication of Ag/Ag2O incorporated graphitic carbon nitride based ZnO nanocomposite for enhanced Z-scheme photocatalytic performance of various organic pollutants and bacterial disinfection. J Environ Chem Eng 2021;9:105996. https://doi.org/10.1016/j.jece.2021.105996.
[99] Chandekar KV, Shkir M, AlFaify S, Al-Shehri BM, Al-Namshah KS, Hamdy MS. A noticeable consistent improvement in photocatalytic efficiency of hazardous textile dye through facile flash combustion synthesized Li-doped ZnO nanoparticles. J Mater Sci Mater Electron 2021;32:3437–50. https://doi.org/10.1007/s10854-020-05090-z.
[100] Shkir M. Green method for synthesis and characterization of copper oxide nanoparticles using Mulberry plant extract and their antibacterial, antioxidant and photocatalytic activity. Phys Scripta 2022;97:105001. https://doi.org/10.1088/1402-4896/ac8a7a.
[101] Haseena S, Shanavas S, Ahamad T, Alshehri SM, Baskaran P, Duraimurugan J, et al. Investigation on photocatalytic activity of bio-treated α-Fe2O3 nanoparticles using Phyllanthus niruri and Moringa stenopetala leaf extract against methylene blue and phenol molecules: kinetics, mechanism and stability. J Environ Chem Eng 2021;9:104996. https://doi.org/10.1016/j.jece.2020.104996.
[102] Vu XH, Phuoc LH, Dien ND, Pham TTH, Thanh LD. Photocatalytic degradation of methylene blue (MB) over α-Fe2O3 nanospindles prepared by a hydrothermal route. J Electron Mater 2019;48:2978–85. https://doi.org/10.1007/s11664-019-07056-2.